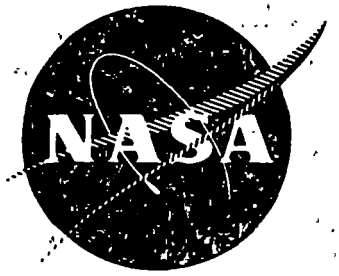

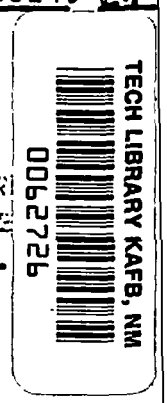

INDUSTRIAL ION SOURCE TECHNOLOGY

PREPARED FOR

LEWIS RESEARCH CENTER

NATIONAL AERONAUTICS AND SPACE ADMINISTRATION

GRANT 3086

Annual Report

November 1976

Harold R. Kaufman
Department of Physics
Colorado State University
Fort Collins, Colorado

1 Report No	2. Government Accession No.	3. Recipient's Catalog No
NASA CR-135149		

4 Title and Subtitle	5. Report Date
INDUSTRIAL ION SOURCE TECHNOLOGY (U)	November 1976
	6. Performing Organization Code

7. Author(s)	8 Performing Organization Report No
Harold R. Kaufman	
	10 Work Unit No

9 Performing Organization Name and Address	11 Contract or Grant No
Department of Physics Colorado State University Fort Collins, Colorado 80523	NSG-3086
	13. Type of Report and Period Covered
12. Sponsoring Agency Name and Address	Contractor Report
National Aeronautics and Space Administration Washington, D. C. 20546	14 Sponsoring Agency Code

15 Supplementary Notes

Project Manager - Elmer Theman
NASA Lewis Research Center
Cleveland, Ohio 44135

16 Abstract

A 30-cm electron bombardment ion source has been designed and fabricated for micromachining and sputtering applications. This source has a multipole magnetic field that employs permanent magnets between permeable pole pieces. An average ion current density of 1 ma/cm^2 with 500 eV argon ions was selected as a design operating condition. The ion beam at this operating condition was uniform and well collimated, with an average variation of ±5 percent over the center 20 cm of the beam at distances up to 30 cm from the ion source.

A variety of sputtering applications were undertaken with a small 10 cm ion source to better understand the ion source requirements in these applications. The results of these experimental studies are also included.

17 Key Words (Suggested by Author(s))	18. Distribution Statement
Ion sources Ion beams Ion micromachining Ion etching	Unclassified - unlimited

19 Security Classif. (of this report)	20. Security Classif. (of this page)	21. No of Pages	22. Price*
Unclassified	Unclassified		

* For sale by the National Technical Information Service, Springfield Virginia 22161

PAGE MISSING FROM AVAILABLE VERSION

CONTENTS

FIGURES

FIGURES (cont.)

FIGURES (cont.)

PART I

THIRTY CM ION SOURCE

Raymond S. Robinson

INTRODUCTION

Slightly modified versions of thrusters have, for several years, been used for industrial ion machining. The performance objectives for surface cleaning, sputtered film deposition, surface texturing and ion machining applications, are high ion current density and a uniform beam current density profile. Because of the differences in performance objectives, modifications of early thruster designs have been only moderately successful. In particular, the ion beams have been excessively peaked and high current densities have required accelerating voltages much higher than desirable for sputtering.

Argon is the usual propellant for sputtering and an ion energy of 500 eV gives a good compromise between material removal and heating and/or damage to the substrate.

The significance of ion energy is indicated in Fig. 1, which shows sputtering yield versus argon ion energy for several materials.[1,2] The sputtering yield initially increases rapidly with ion energy. Above about 300 to 500 eV, though, the yield increases much more slowly with ion

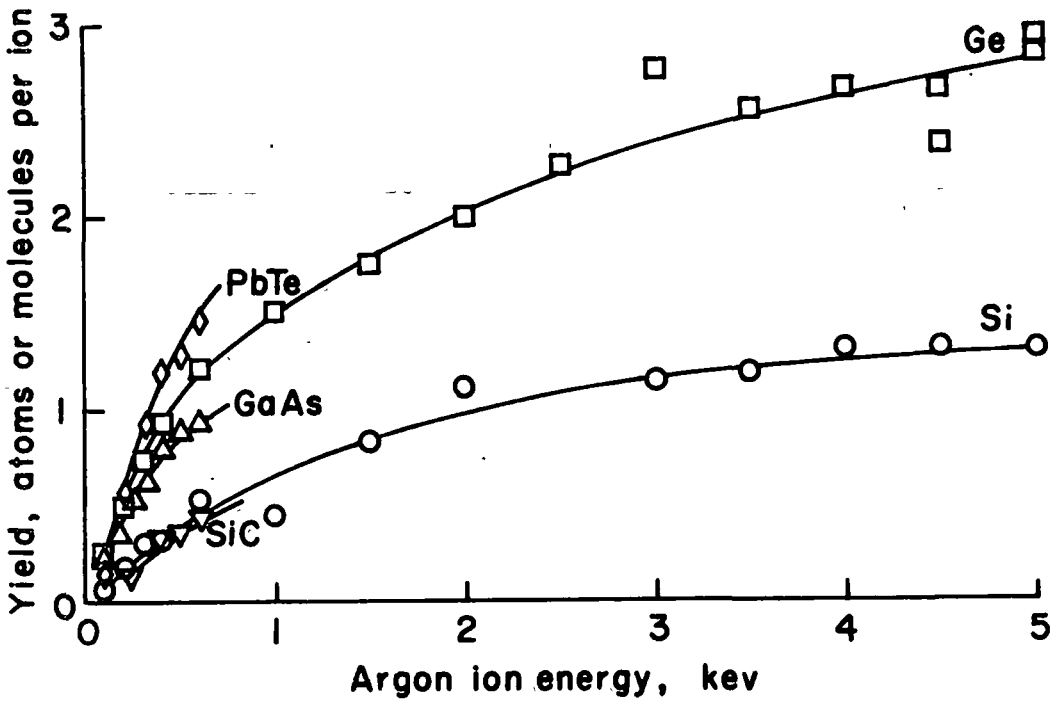

Figure 1. Sputtering yield of several materials to normal incidence argon ions.

energy. The minimum heating and surface damage for a given amount of material removal is thus found in the 300-500 eV range for most materials. A design value of 500 eV appears to be a reasonable compromise to minimize the required perveance of the accelerator system. This line of reasoning is believed to be behind the widespread use of 500 eV argon ions to machine solid-state devices.

Wider application of ion machining as a production technique will require larger ion sources than those presently available. The 30-cm beam diameter used herein represents a substantial increase over previous sources used in these applications. It is also about the largest ion beam that can be conveniently generated in the widely available 45 cm size bell jar.

The design conditions selected for this 30-cm ion source were 1 ma/cm^2 of 500 eV argon ions. The beam should also be uniform and well-collimated so that a high ion current density can be used at large distances from the ion source. An increased distance from the source to the target, of course, decreases mutual sputtered contamination of the target and the ion source.

To meet these design criteria, modifications are required in both the ion chamber and the accelerator system from customary thruster designs. Recent developments suggest a flat multipole chamber with multiple cathodes is the proper discharge chamber approach for a uniform ion beam - as opposed

to the near axial magnetic field used to date in modified thrusters.

An ion thruster with a multipole magnetic field is reported by Isaacson and Kaufman.[3] This design is conceptually related to both the multipole approach of Moore[4] and Ramsey,[5] and the cusped field approach of Beattie and Wilbur.[6] The early multipole design of Moore and Ramsey used permanent magnets with very high field strengths directed into the ion chamber. The current multipole designs are more closely related to the lower field cusped design of Beattie and Wilbur that uses soft iron pole pieces to direct the magnetic flux for primary electron containment. The major departures of the 30-cm source described herein from the design of Isaacson and Kaufman were the use of permanent magnets rather than electromagnets between the pole pieces and the large increase in discharge chamber diameter.

EXPERIMENTAL APPARATUS

Testing facilities include a 1.2 m diameter, 4.6 m long vacuum facility pumped by an 0.8 m oil diffusion pump together with associated instrumentation and power supplies. The vacuum chamber has a cryogenic liner cooled by liquid nitrogen. A 45 cm bell jar vacuum facility, with associated power supplies, was also used in this investigation.

Due to the size, weight, and preferred orientation of the 30-cm source, it was not possible to support it, in the manner customary of smaller thrusters, cantilevered through the valve in the vacuum system. A special support table was built onto the large (1.2 m) swinging door at the end of the test chamber. The entire ion source was surrounded with a cylindrical structure covered by stainless steel screen to isolate the high voltage surfaces of the ion source from the charge-exchange plasma generated by the ion beam.

A set of three Faraday probes was fabricated to measure beam current density 10 cm, 20 cm, and 30 cm downstream of the grids. A probe consisted of a 0.64 mm diameter molybdenum collecting disk mounted in, but electrically isolated from, a stainless steel ground plane. The collecting surface was biased 24 v. negative of the ground plane to repel electrons and allow the collection of ion current.

DISCHARGE CHAMBER

A cylindrical discharge chamber was selected with an inside diameter of 30-cm and a depth of 10 cm. A radial cross-section of the 30-cm discharge chamber showing construction details is shown in Fig. 2. A multipole discharge chamber will generally produce a more uniform ion beam current density profile as the chamber is decreased in depth, however, the minimum working gas pressure inside the chamber required for operation will increase as chamber depth is decreased. Data obtained by Isaacson and Kaufman[3] showed these trends down to a chamber depth equal to about half of the 15-cm diameter used in their investigations. The absence of any further improvement in uniformity for smaller depths was felt due, in part, to the close proximity of the central refractory cathode to the accelerator system. With the circumferential cathode employed in the 30-cm source, a further decrease in depth was expected to improve beam uniformity for the larger source. A chamber depth equal to one third of the 30-cm diameter was therefore selected.

A 30-cm discharge chamber diameter, together with anodes, pole pieces, and other required hardware, results in an overall ion source diameter of about 42 cm. Thus, a 30-cm ion beam is about the largest that can conveniently be generated with the entire source still fitting inside a 45-cm diameter bell jar.

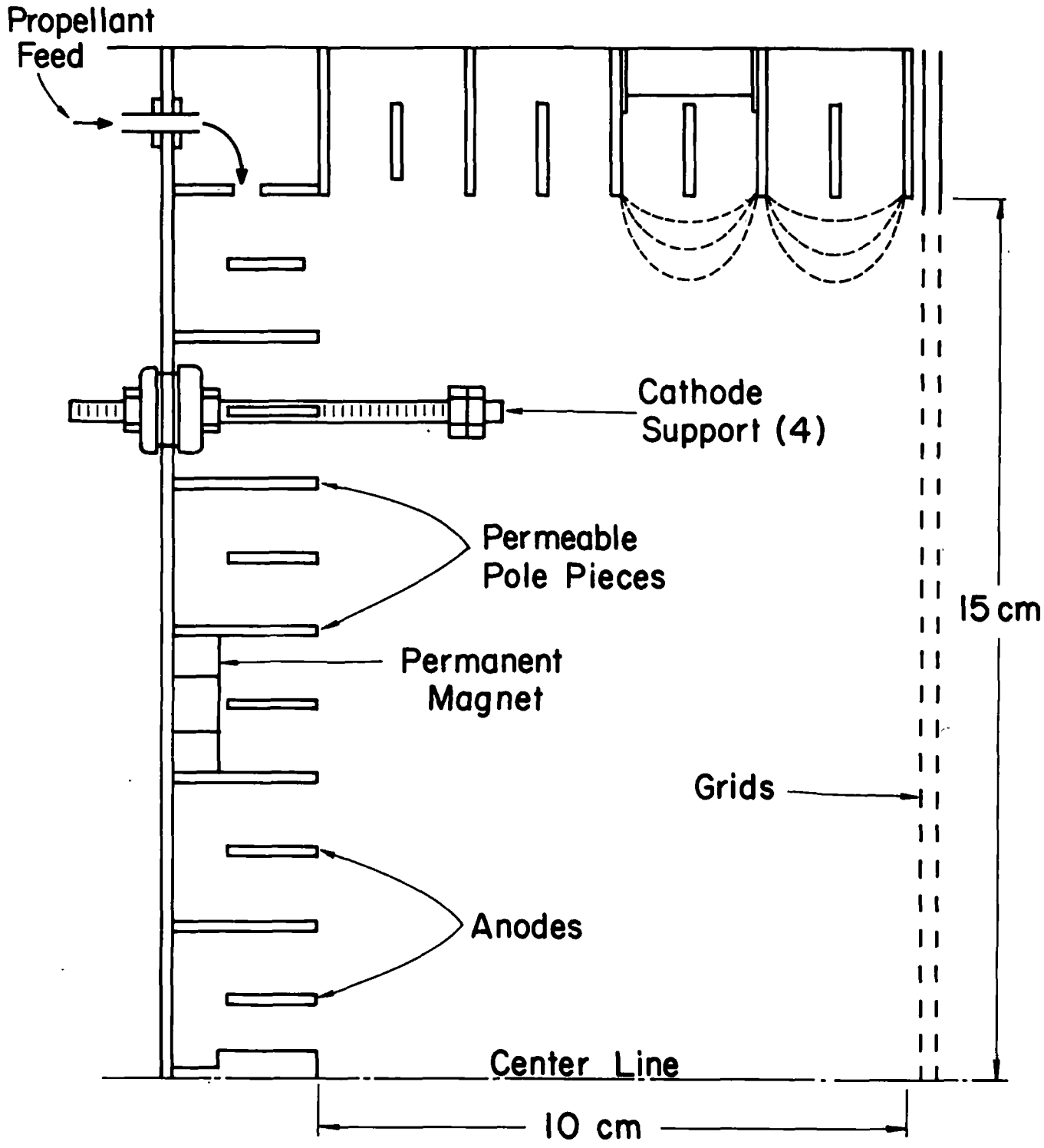

Figure 2. Radial cross section of a 30-cm ion source.

MAGNETIC CIRCUIT

The magnetic field in the source was provided by 139 Alnico V permanent magnets. The permanent magnets were cut from 15-cm rod stock 6.4 mm in diameter and finished to a length of 2.38 cm. A fraction of the magnetic field strength is lost in the machining process but this mild degradation was not felt to be serious. Along the side of the discharge chamber, the permanent magnets were held in position between the pole pieces by 0.5 mm "U"-shaped stainless steel retainers. The five side pole pieces themselves were annular disks of 30.5 and 35.6 cm inside and outside diameters. The 1.5 mm thick low carbon steel pole pieces were spaced about 2.5 cm apart. There are twenty permanent magnets between each pair of pole pieces on the sides for a total of eighty magnets in these locations.

The pole pieces on the upstream end of the discharge chamber are rolled cylinders of 1.5 mm thick, low carbon steel with a single welded joint reinforced with stainless steel. The center pole piece was a solid cylinder, which was required to have a diameter of 9.5 mm to avoid saturation. A thinner center pole piece had to be replaced to avoid severe distortion of the magnetic field. All hardware at the upstream end is mounted on an aluminum plate 3.2 mm thick and 35.6 cm in diameter. The upstream permanent magnets are held down with 0.25 mm stainless steel brackets. On the upstream end, beginning at the center, there are two,

five, eight, twelve, fourteen, and eighteen magnets between adjacent sets of pole pieces for a total of fifty-nine magnets.

The sense of the magnets surrounding the discharge chamber is such that the magnetic polarity of adjacent pole pieces is opposite. An example of the magnetic field lines in the fringe field between pole pieces is shown schematically by dotted lines in Fig. 2. An essential feature of this multipole design is that the fringe field falls off very rapidly with increasing distance from the pole pieces, so that the magnetic field is negligible over most of the discharge chamber volume. This results in relatively free access to this volume by primary electrons, which would be expected to give a more uniform plasma density.

ANODES

Ten 1.5 mm thick stainless steel anodes are located at equal spacings along the side and upstream end of the discharge chamber. Each anode is midway between the two neighboring pole pieces (see Fig. 2). Like the pole pieces, the four side anodes are flat, annular disks and the six upstream anodes were rolled cylinders, ranging from about 2.5 cm to 28 cm in diameter. All but two of the anodes have inner edges flush with those of the adjacent pole pieces. The two corner anodes are recessed about 2.5 mm. The reasons for this recess are discussed in the following section. A cylindrical shroud of 0.25 mm stainless steel seals the sides of the discharge chamber. The side and upstream anodes are held by aluminum oxide isolating supports mounted on this shroud and on the upstream aluminum end plate.

REQUIRED MAGNETIC FIELD STRENGTH

In the multipole design, a fringe magnetic field adjacent to the anodes prevents the escape of primary electrons directly to the anodes before expending most of their energy in the production of ions. In calculating the deflection of an electron in such a fringe field, it is assumed that the radius of curvature of the anode is large compared to the depth of the fringe field. It is further assumed that the magnetic induction $\vec{B}$ is parallel to the anode and that its magnitude varies only as a function of the distance from the anode.

In passing through an infinitesimal region dx, an electron with a component of velocity v normal to $\vec{B}$ is deflected through an angle $d\theta$, as indicated in Fig. 3. The radius of curvature for the electron trajectory in the region dx is

$$r = mv/q\ B(x) \quad ,$$

where m and q are the mass and charge of an electron. In Fig. 3., x represents the penetration depth of the electron into the fringe field from the field free region. The radius of curvature r can be related to $d\theta$ and dx through geometrical considerations,

$$rd\theta = dx/\sin\theta \quad .$$

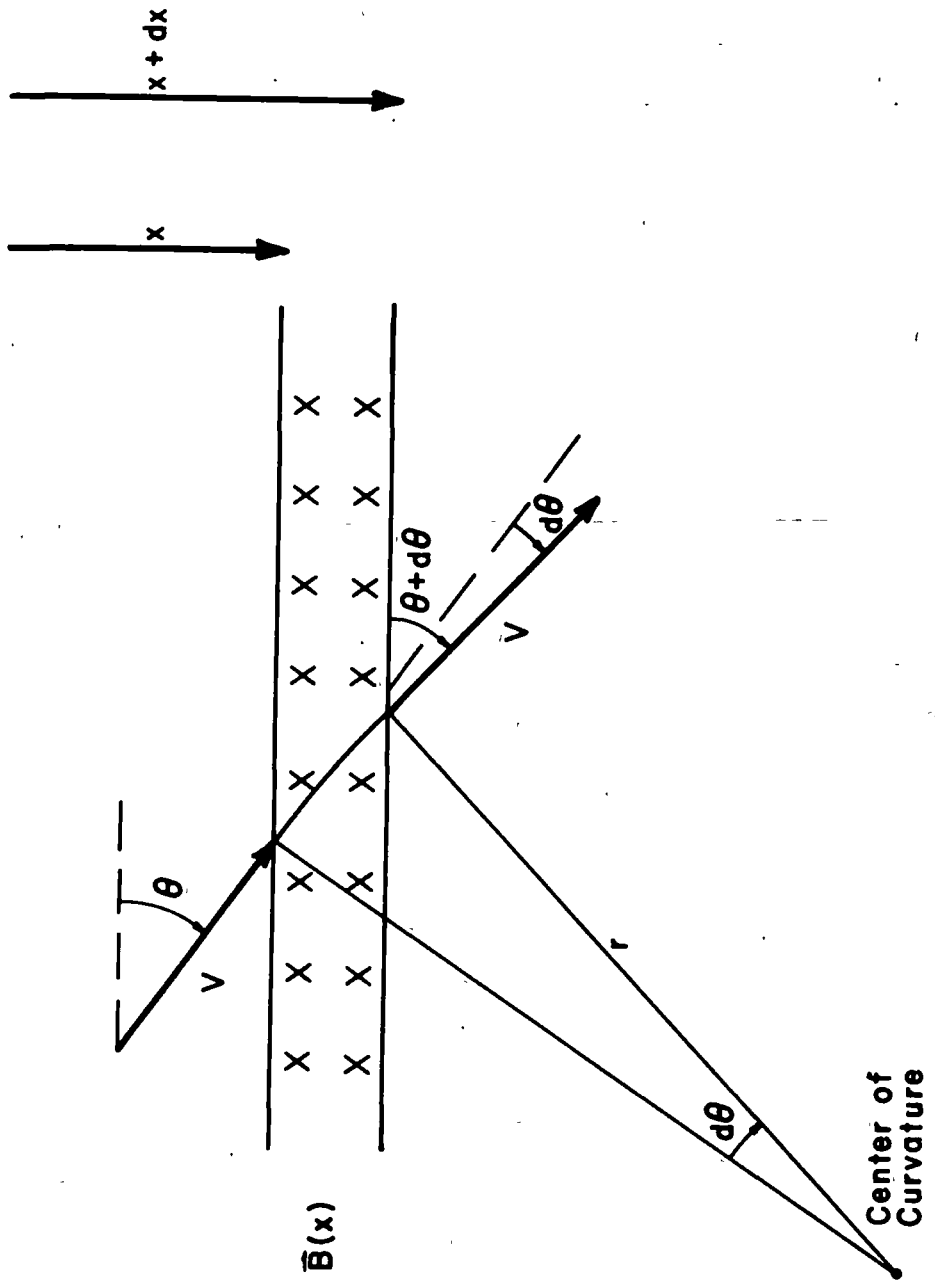

Figure 3. Electron deflection in magnetic field.

Combining the last two expressions to eliminate r,

$$B(x)dx = \frac{(mv)}{q} \sin\theta d\theta \ .$$

The integral of $B(x)dx$ can be related to the electron deflection by

$$\int_0^D B(x)dx = \int_{\theta_i}^{\theta_f} \frac{mv}{q} \sin\theta d\theta \ ,$$

where θ_i is the angle of incidence of the electron from the field free region and θ_f is the trajectory angle after the electron traverses a thickness D of magnetic induction. The maximum value of the angular integral corresponds to the maximum possible electron penetration toward the anode, and is obtained with θ_i equal to zero and θ_f equal to π. For these limits,

$$\int_0^D B(x)dx = 2mv/q \ .$$

In terms of electron kinetic energy E,

$$\int_0^D B(x)dx = \frac{8m\ E}{q^2}^{\frac{1}{2}} \ .$$

With the substitution for electron charge and mass, this becomes

$$\int_0^D B(x)dx = 6.74 \times 10^{-6}\ E^{\frac{1}{2}} \ ,$$

where E is in electron-volts and the left-hand side is in SI units. This expression provides a criterion for primary electron containment by the integrated magnetic field.

Primary electrons have long mean free paths and are not likely to undergo strong deflection from the indicated trajectory while in the fringe field region. Low energy Maxwellian electrons, however, have much shorter path lengths and are more likely to migrate across the fringe field region (by collision) to be collected at the anode, thus sustaining the discharge current.

For 50 eV primary electrons, an integrated magnetic field of 48 Gauss-cm is indicated by the preceding equation. To allow for several factors not included in this simple derivation, the 30-cm source was designed for an integrated field approximately 50 percent larger than this value.

Although this derivation did not specifically take into account the strong curvature of the magnetic field lines along some of the possible directions of approach to an anode, it is felt that the criterion provided for the integrated magnetic field is still valid because circulating charged particles in regions of magnetic field enclose within their orbits a constant amount of magnetic flux which depends on the charge and momentum of the particle. Thus, there would seem to be a critical magnetic field line beyond which an electron would not penetrate toward the anode for a given electron energy, regardless of the direction of approach.

Figure 4 shows a typical variation of magnetic field strength midway between two pole pieces. The plane of measure-

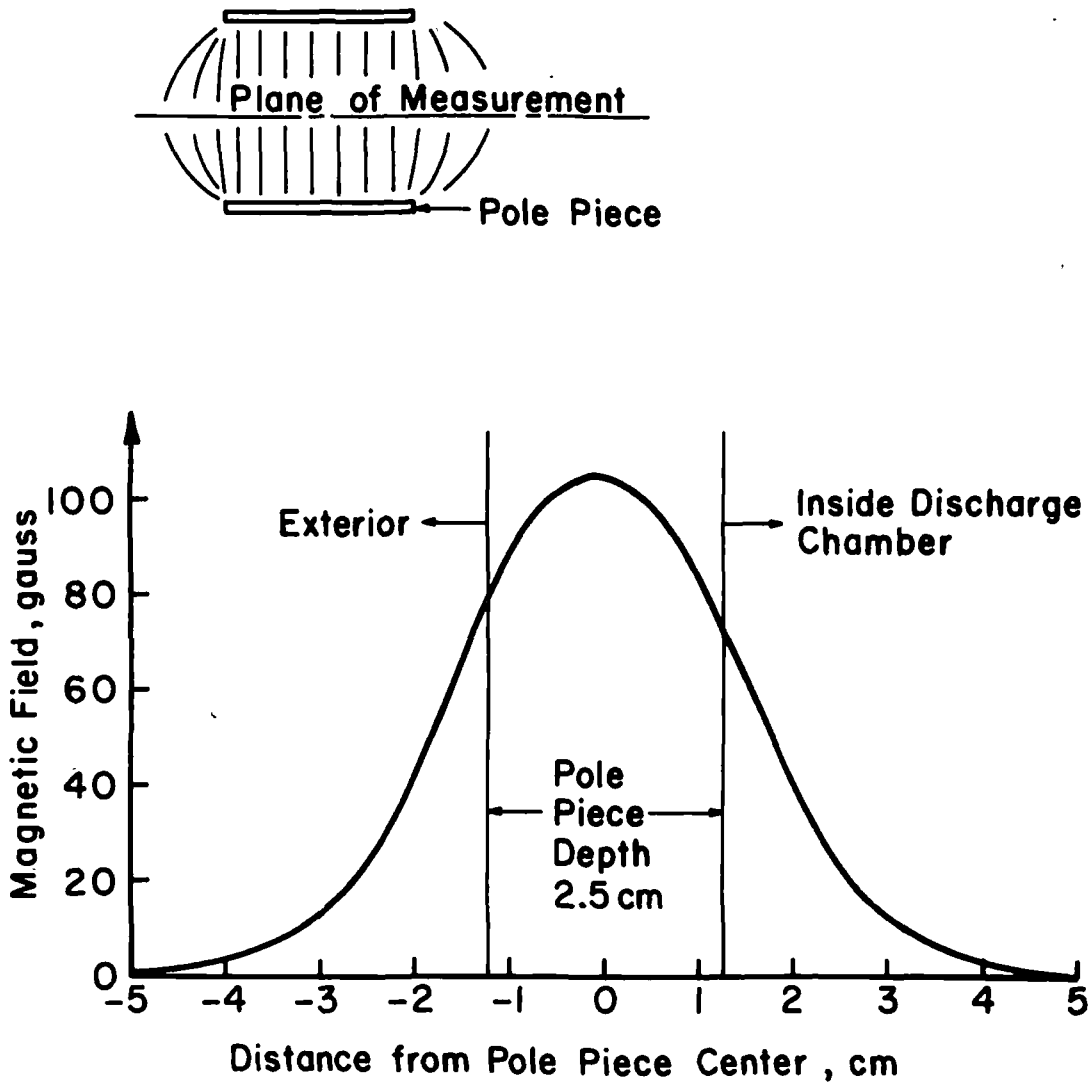

Figure 4. Variation of magnetic field midway between two pole pieces.

ment is shown in the insert at the top of the figure. The magnetic field integral of interest would be the area under the curve from the inside field free region to the edge of the anode. A least squares curve fit was obtained for the interior fringe field:

$$B(y) = 106\ e^{-0.235(y + 1.27)^2} ,$$

where y is the distance in cm from the anode edge and $B(y)$ is in Gauss. Using the least squares fit to the magnetic field and integrating the equations of motion for an electron using a fourth-order Runge-Kutta method, a deepest penetration trajectory was obtained for a 45.5 eV electron. This trajectory is shown in Fig. 5.

For each anode location, the actual measured magnetic field was numerically integrated from the inner edge of an anode out to the nearly field free region in the discharge chamber. In most cases, the inner edge of the anode was flush with the inner edges of the two neighboring pole pieces. The two corner anodes, however, were recessed 2.5 mm behind neighboring pole pieces. The recessing of corner anodes had been found earlier to be a convenient solution to the corner problem of the multipole discharge chamber.[3] The 2.5 mm recess used herein resulted in an increase of about 18 Gauss-cm for the field integrals for the corner anode locations. Without this increase, the integrals for the corner anodes would have been substantially smaller than the integrals for the other anodes.

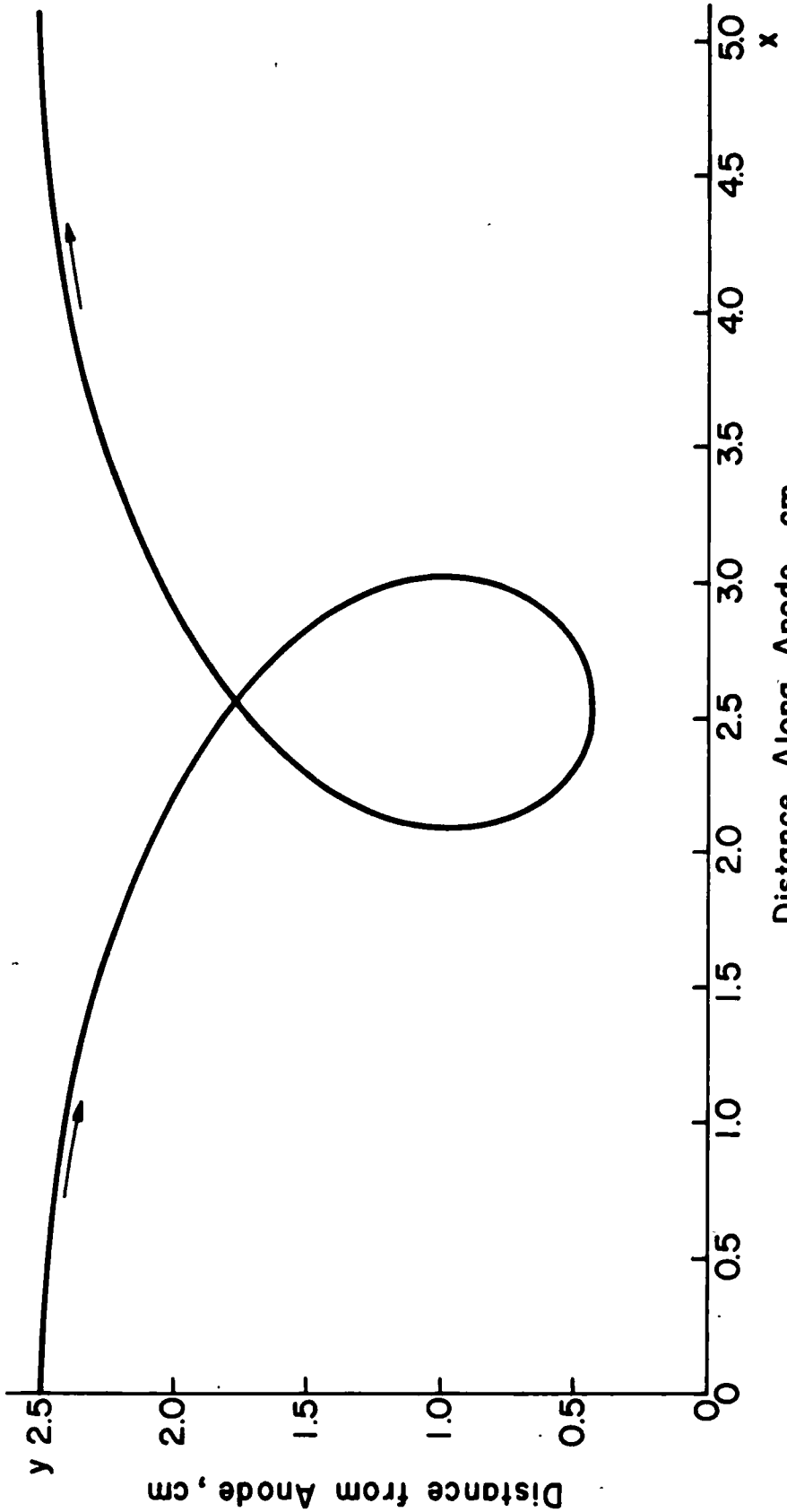

Figure 5. Computed electron trajectory in fringe field region.

The final magnetic field integrals at the ten anode locations are shown in Fig. 6. The average is about 77 Gauss-cm, while the minimum is about 67 Gauss-cm at anode number 7 (a corner anode). The placement and, more importantly, the number of permanent magnets between each set of pole pieces was selected to give uniformity of the magnetic field and of the integral of the field at the anode locations (Fig. 6). While adequate uniformity was obtained with uniform spacing of the side magnets, the upstream magnets required more of a cut and try approach, especially where small numbers of magnets were used between pairs of pole pieces. The final arrangement for these upstream magnets is shown in Fig. 7(a). Note that the magnets in neighboring sections were staggered to avoid local saturation of the pole pieces. The magnets in the side sections were also staggered, although in a more regular manner.

Figures 7(b) and 7(c) show the magnet placement in the sides and the location of the anodes between adjacent pole pieces.

The nature of magnetic flux spreading between pole pieces from discrete sources of flux (permanent magnets) was investigated. The magnetic field was measured at constant depths between pole pieces at points around the circumference of the chamber separated azimuthally by five degree increments. Measurements were taken at two depths, (1) at the center between pole pieces and (2) flush with the inner pole piece

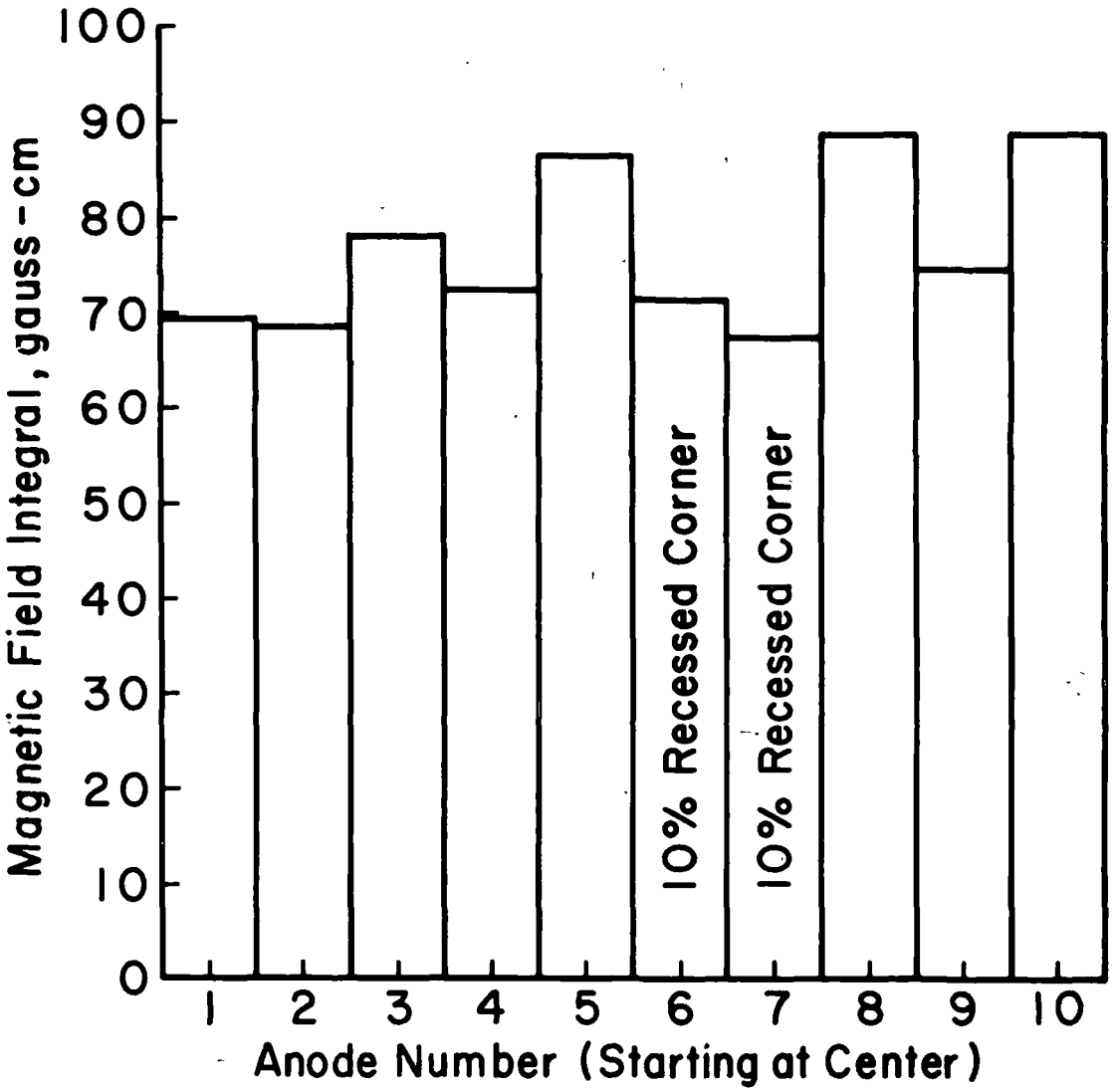

Figure 6. Magnetic field integrals above the anodes.

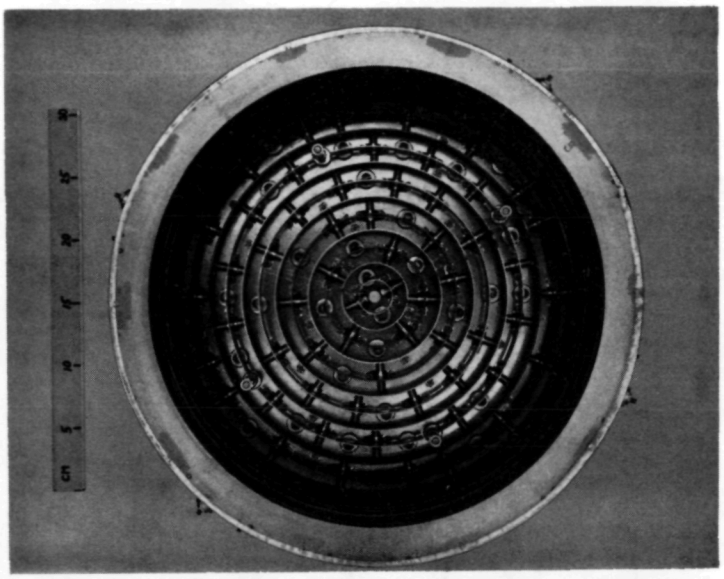

Figure 7. (a) Upstream end of 30-cm discharge chamber (inside view).

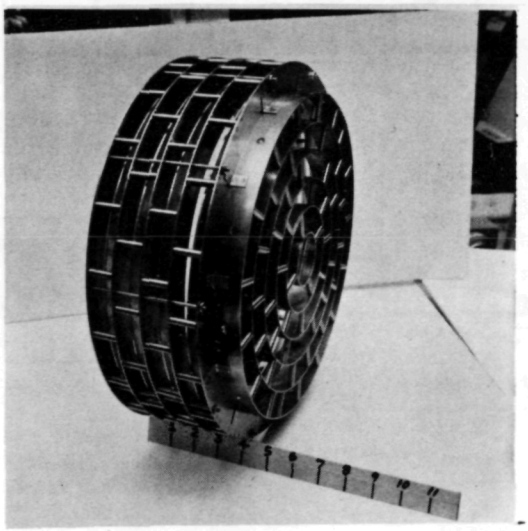

Figure 7. (b)

Outside wall upstream end of 30-cm discharge chamber.

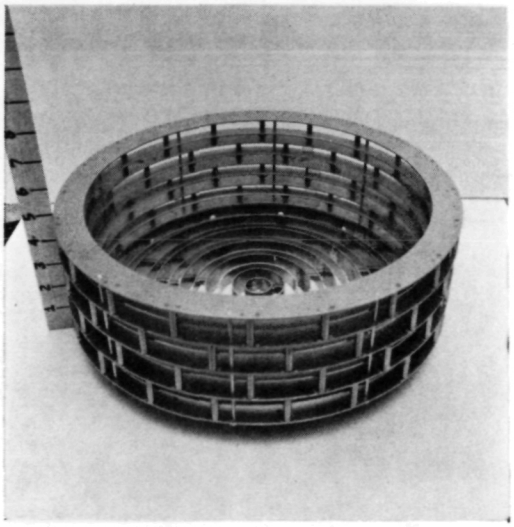

Figure 7. (c)

Oblique view of 30-cm discharge chamber.

edges. These measurements were taken for each of the ten pairs of pole pieces. Figure 8 shows the measurements at the location of anode 9. Extremely sharp variations in field strength are observed in the center between the pole pieces, however, when measurements are taken flush with the inner edge of the pole pieces, the azimuthal uniformity is very good indicating that the flux distribution is quite uniform in the pole pieces at distances of the order of 2 cm from the flux sources. For a configuration similar to the one used, then, flux uniformity can be assumed at the inner edges of the pole pieces.

Given the inherent uncertainty of magnetic circuit design, any known consistencies in field behavior are of some interest. Figure 8 shows azimuthal field variations in the center between the pole pieces. This field varies rapidly over a wide range, but a mean field can also be calculated. Table 1 gives the calculated means for two locations at each anode. The largest mean at a given location (center or flush) can be as much as 67% greater than the smallest, but the variation in the ratio of the two locations at a given anode is much smaller. This would seem to indicate that pole piece geometry governs the variation of field with distance, independent of field magnitude.

The upstream end and the sides have significantly different magnetic circuit geometries but a consistent factor in the design of both was the magnitude of the field integrals.

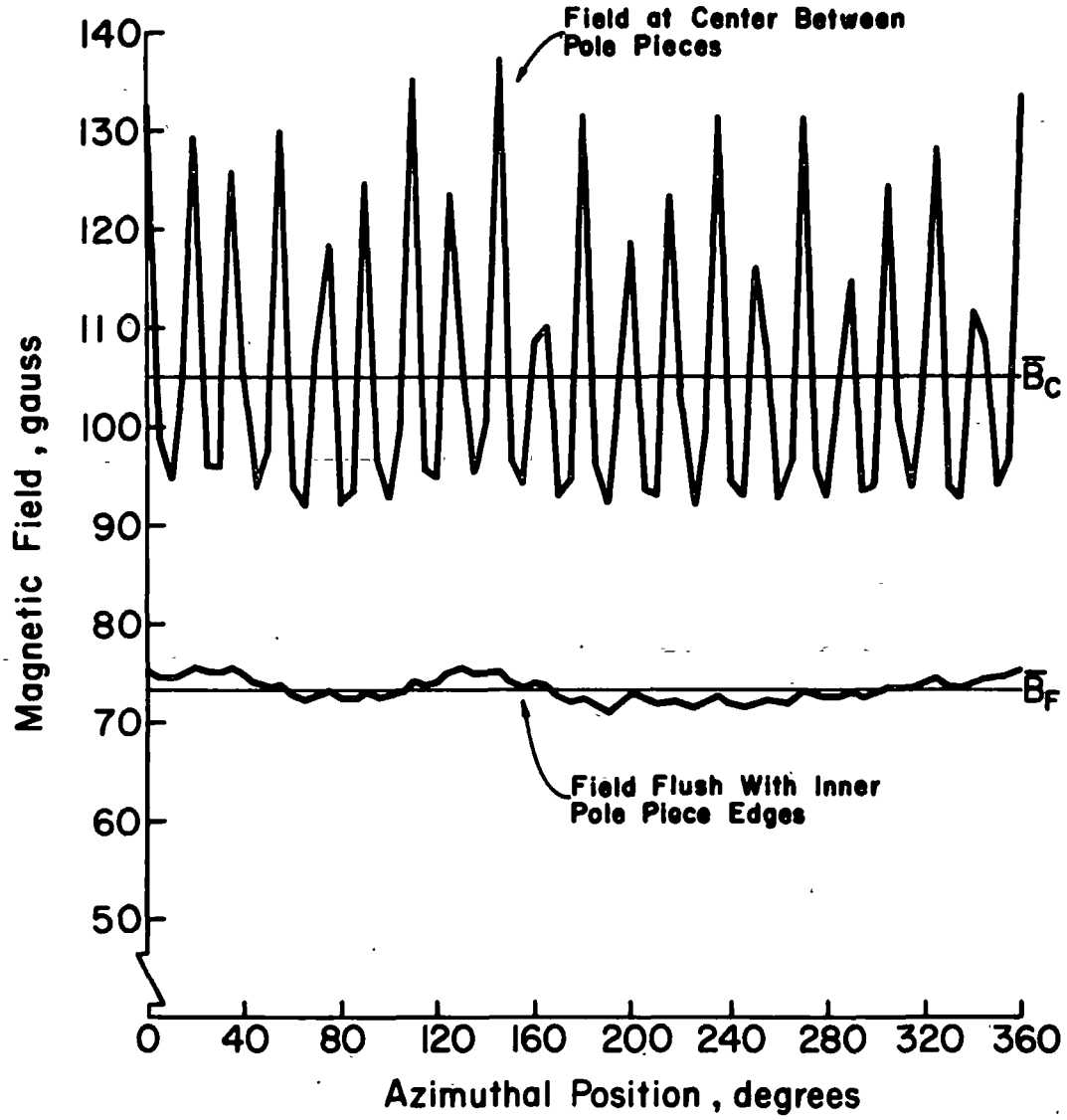

Figure 8. Azimuthal variation of magnetic field between pole pieces.

Table 1. Fields Averaged over Azimuthal Position.

Location	$\bar{B}_{Flush}$	$\bar{B}_{Center}$	$\bar{B}_F/\bar{B}_C$
1	99.6 Gauss	131.2 Gauss	.76
2	72.3	105.4	.69
3	76.2	110.7	.69
4	73.3	108.2	.68
5	74.3	103.9	.72
6	70.6	96.6	.73
7	61.3	87.0	.70
8	73.6	105.9	.69
9	73.3	104.9	.70
10	65.0	91.5	.71

Table 2 shows the parameter magnets per unit length of anode for the ten anodes. This parameter is quite consistent from

Table 2. Magnets per cm of Anode.

Anode	Magnets	Magnets/cm of anode
1	2	0.25
2	5	0.21
3	8	0.20
4	12	0.21
5	14	0.20
6	18	0.21
7	20	0.21
8	20	0.21
9	20	0.21
10	20	0.21

anode to anode, deviating most for the section with only two magnets.

Figures 9(a) and 9(b) show the completed discharge chamber with the outer shroud and upstream end plate in place. Note the high density of mounting hardware and insulators attached to the upstream end plate.

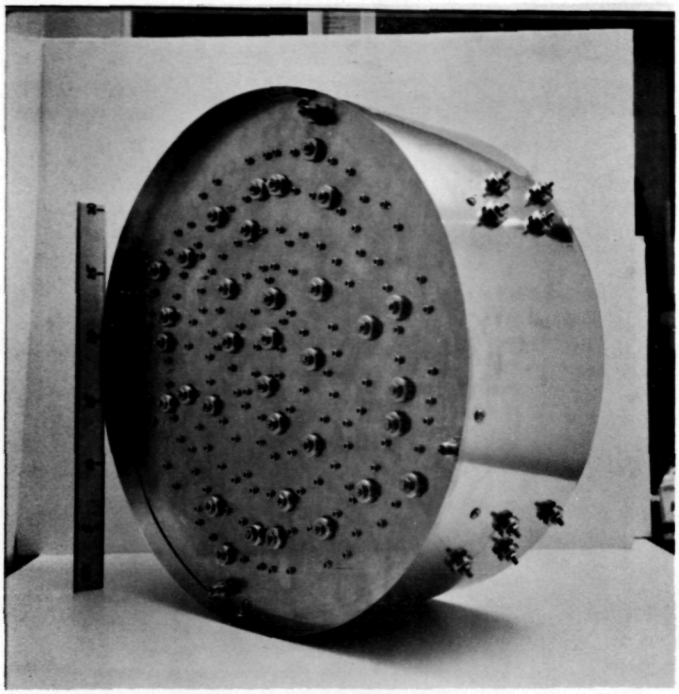

(a) Back

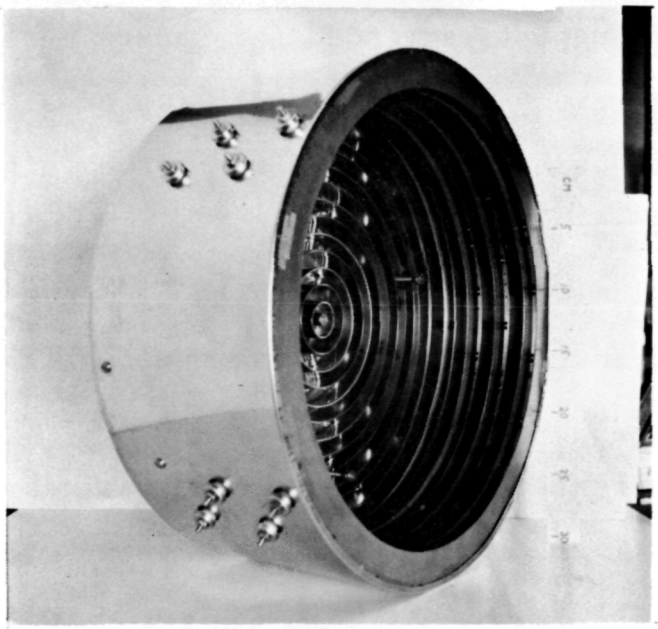

(b) Front

Figure 9. Completed 30-cm discharge chamber.

CATHODES

Refractory metal cathodes of 0.25 mm tantalum wire were used for both the discharge chamber and the neutralizer. The periodic maintenance of thermionic emitters is not a major problem in ground applications. On the other hand, the extended emission surface of a wire discharge chamber cathode can be a definite advantage in obtaining a more uniform beam profile.

Tungsten wire could have been used instead of tantalum, but tantalum was preferred because of its greater ductility.

The discharge chamber cathode was made in the shape of a square, held at the corners by four insulated supports extending through the upstream end of the chamber (see Fig. 2). The cathode supports extended far enough into the discharge chamber to prevent thermionic emission of electrons directly into the fringe magnetic field where they might be lost directly to the anodes.

Electrical connections were made to the cathode corners so that the four side sections were effectively in parallel. Cathode placement was selected to enhance beam uniformity. The circumferential cathode employed was near the side (cylindrical) wall of the discharge chamber to help offset the decrease in plasma density usually found in that location. It was also located nearer the upstream end of the chamber to permit the use of a very flat chamber without the sharp

peaks in beam current density that are often found when a cathode is close to the accelerator system.

A single strand neutralizer cathode was stretched across the diameter of the beam about 5 cm from the accelerator system. The ends were triple wrapped to limit the emission length to 30-cm across the center of the beam. The neutralizer insulating supports were kept about 6 cm from the edge of the beam to prevent unnecessary contamination of the beam.

Neutralization was obtained with an ion beam by increasing the heating current until no net current was measured to a grounded Faraday probe in the center of the beam 10 cm from the accelerator grid.

Both the discharge chamber cathode and the neutralizer cathode were heated with 60 Hz current. The center tap of the discharge chamber cathode heater winding was at the potential of the discharge chamber outer shell. The neutralizer heater center tap was grounded. Low resistance between ground and the neutralizer secondary center tap is required if neutralization is to be obtained in this manner without a neutralizer bias voltage.

ACCELERATOR SYSTEM

The 30-cm ion source was tested with two different accelerator systems. One system used flat carbon grids, while the other used dished molybdenum grids.

The carbon grids were fabricated from dense, fine grained carbon (Union Carbide, Grade ATJ). The holes were drilled in a close packed hexagonal pattern with 4.1 mm between centers. The screen holes were 3.3 mm in diameter (57 percent open area), while the accelerator holes were 2.6 mm in diameter (37 percent open area). Both grids were 1.5 mm thick, but the beam area of the screen (30 cm diameter) was milled down to a thickness of 0.76 mm.

Ion optics data from Aston and Kaufman[7] were used to determine the optimum spacing between grids. For minimum beam divergence at 1 ma/cm^2 of 500 eV argon ions, this spacing was calculated at 1.7 mm for the carbon grid geometry. Grid elasticity, however, was also found to be a problem. In the usual horizontal grid position (ion beam directed downwards), the screen was found to sag 1 mm closer to the accelerator in the center than at the edge of the beam. Further, with the screen 50^{o}C hotter than the accelerator, thermal expansion would account for the rest of the 1.7 mm spacing. Experimentally, severe high voltage arcing was encountered in the center of the grids after a short operating time. Because of these limitations, a

separation of 2.5 mm was used for the carbon grids. A circular frame was designed to support both the ion source body and the accelerator system grids. This support was configured so that the weight of the ion source body did not rest on the grids.

Figure 10 is a photograph of the accelerator grid of the carbon grid set after a few hours use. The grid is shown mounted to the aluminum support ring described above.

Figure 11 is a closeup of these same grids. Some of the holes have a ragged appearance around the edges. This effect is possibly due to problems with grid fabrication or some process of accumulating sputtered material on the grid. The light-colored areas are an aluminum coating which has been sputtered from an aluminum target placed in the beam. The dark, triangular areas appear to be locations of preferential re-etching of the aluminum film by charge exchange ions impinging on the accelerator grid.

A set of dished, compensated molybdenum grids,was supplied by NASA Lewis Research Center. The screen grid was fabricated of 0.38 mm thick molybdenum with 1.9 mm holes on 2.2 mm centers (67% open area). The accelerator grid was 0.51 mm thick with 1.6 mm holes (43% open area). The grids were dished outwards from the discharge chamber, with a dishing depth of about 2.5 cm. The hole pattern for these grids was within a 28 cm diameter.

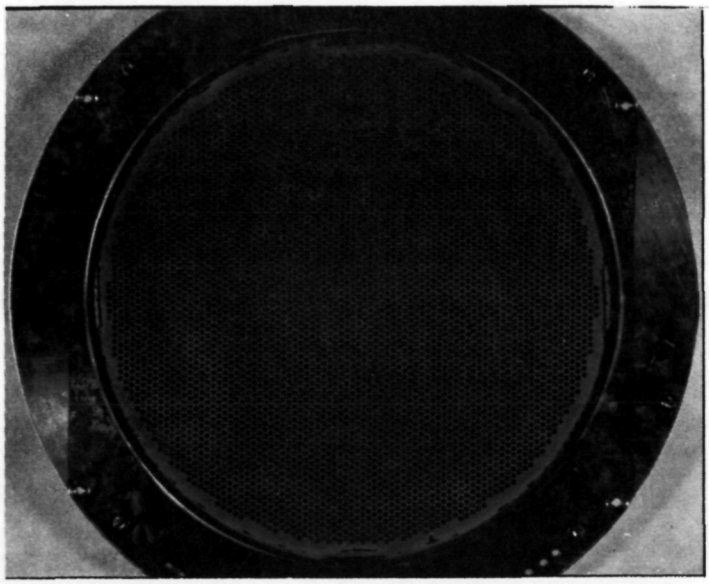

Figure 10. Carbon accelerator grid after few hours use.

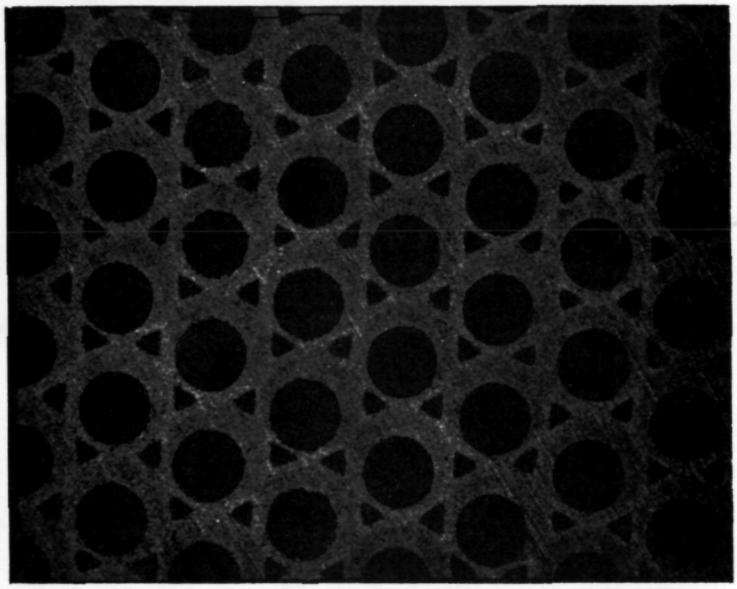

Figure 11. Closeup of carbon accelerator grid.

Because of the dishing, the ion beam would be strongly divergent if the spacing between the holes were the same for both grids. To deflect the beamlets back toward the axial direction, the grids are compensated, that is, the spacing between holes is made slightly larger in the accelerator grid. The resulting hole displacement and beamlet deflection is indicated in Fig. 12.

Using the same ion optics data,[7] a grid separation of 1.7 mm was also indicated for minimum beam divergence at 1 ma/cm^2 of 500 eV argon ions for the dished molybdenum grids. The accelerator system functioned well at this spacing. It also functioned well at a reduced spacing of 0.84 mm, with no visual or operational indications that the spacing was too close.

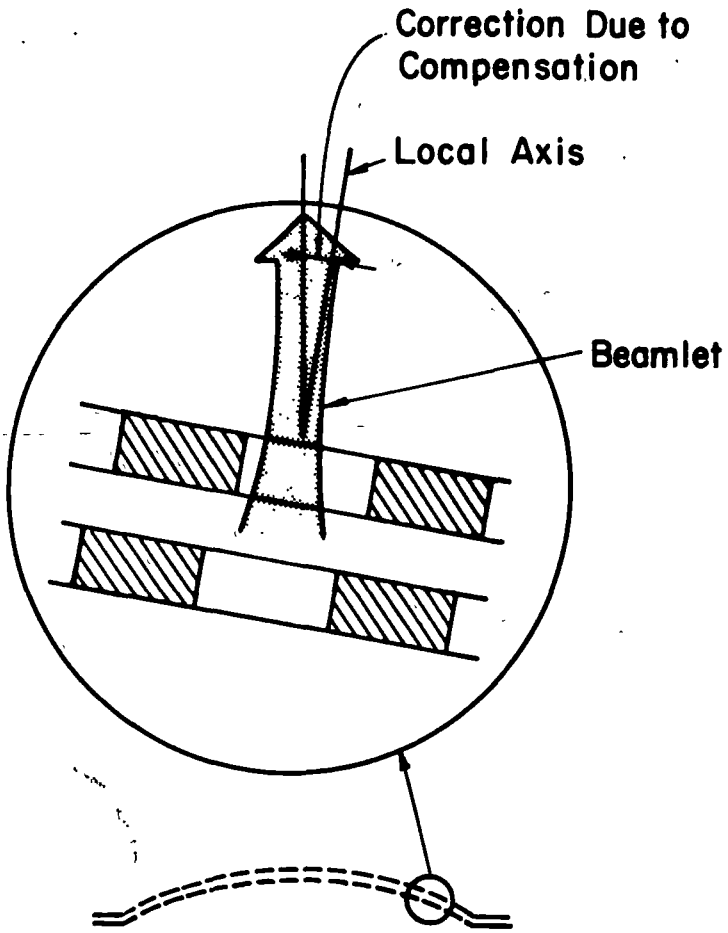

Figure 12. Deflection of beamlet toward axial direction by compensated grids.

PROPELLANT INTRODUCTION

For operation in the large vacuum facility argon gas was fed directly to the discharge chamber through twelve equally spaced 5 mm diameter ports in the upstream corner pole piece. These ports are indicated in Fig. 2, and can also be seen in the photograph in Fig. 7(b). Argon was introduced into the annular region in the upstream corner through four feed lines in the upstream end plate. Propellant flow rate was controlled using a needle valve and monitored with a Hastings mass flow meter.

In the 45-cm bell jar vacuum facility, propellant was introduced directly into the bell jar rather than through the feed ports. The pressure inside the discharge chamber then was assumed to be approximately equal to the pressure in the bell jar.

INITIATION OF DISCHARGE

The 1.2 m diameter vacuum chamber could be pumped down to 3×10^{-6} Torr in the absence of argon flow. When the ion source was installed in this chamber, the discharge was initiated by increasing the argon flow to a high value - high enough to cause severe arcing if the high voltage was applied without reducing the argon flow. Starting procedure also included increasing the discharge voltage from the normal 50v to 62v and temporarily increasing the ion source shell to anode potential. Both increasing the discharge voltage and providing more surface at anode potential (not protected by magnetic fields) tended to increase the initial space-charge-limited electron emission thus initiating a discharge. Normal source operation was at both 900 mA-equivalent argon flow (about 1×10^{-5} Torr facility pressure) and 1500 mA-equivalent argon flow (about 1.5×10^{-5} Torr facility pressure). Attempts to maintain a discharge while lowering the argon flow rate to 600 mA-equivalent were not successful.

Initiation of the discharge, while operating in the bell jar, did not require increasing the flow above the normal operating value.

DISCHARGE CHAMBER PERFORMANCE

Discharge chamber performance was compared for the two accelerator systems tested. Keeping all operating parameters the same except the optics, Fig. 13 shows that lower discharge losses were obtained with the molybdenum grids over most of the operating range. This performance difference was attributed to the larger open area fraction of that screen grid. On the other hand, slightly higher propellant utilization could be obtained with the carbon grids, which was attributed to the smaller open area fraction of that accelerator grid. The propellant utilization was uncorrected for both double ionization and propellant backflow from the facility. Even with allowances for these corrections, the attainable utilizations appear reasonable for ground applications. The level of discharge losses is quite low for ground applications and quite impressive considering that no changes were necessary in the discharge chamber to reach this performance level.

Variation of discharge chamber performance with propellant mass flow rate was also observed. For a given accelerator system, while holding the screen, accelerator and discharge voltages fixed, a decrease in discharge power loss was found with increased propellant mass flow rate. Figure 14 shows the decrease in discharge loss as the propellant mass flow rate is increased from 900 ma-equiv. to

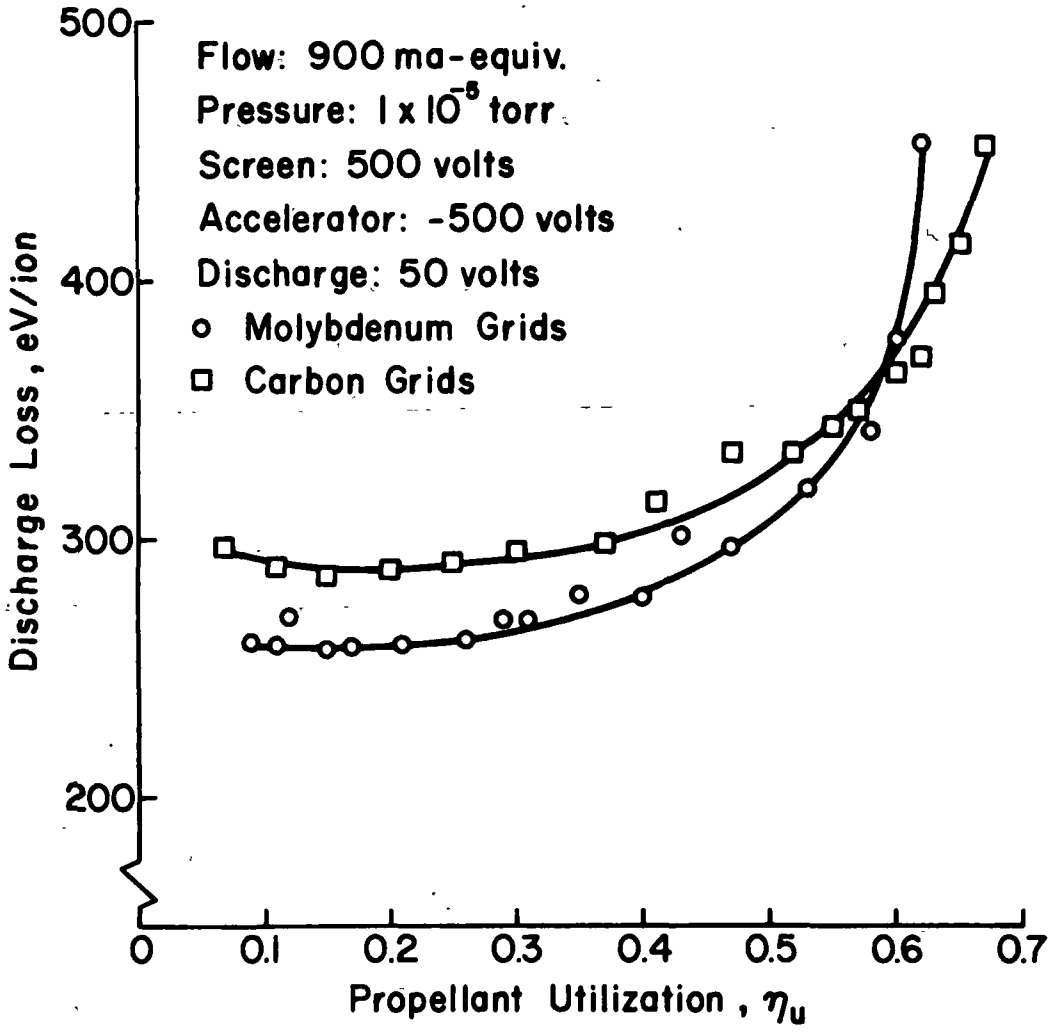

Figure 13. Discharge chamber performance for two accelerator systems.

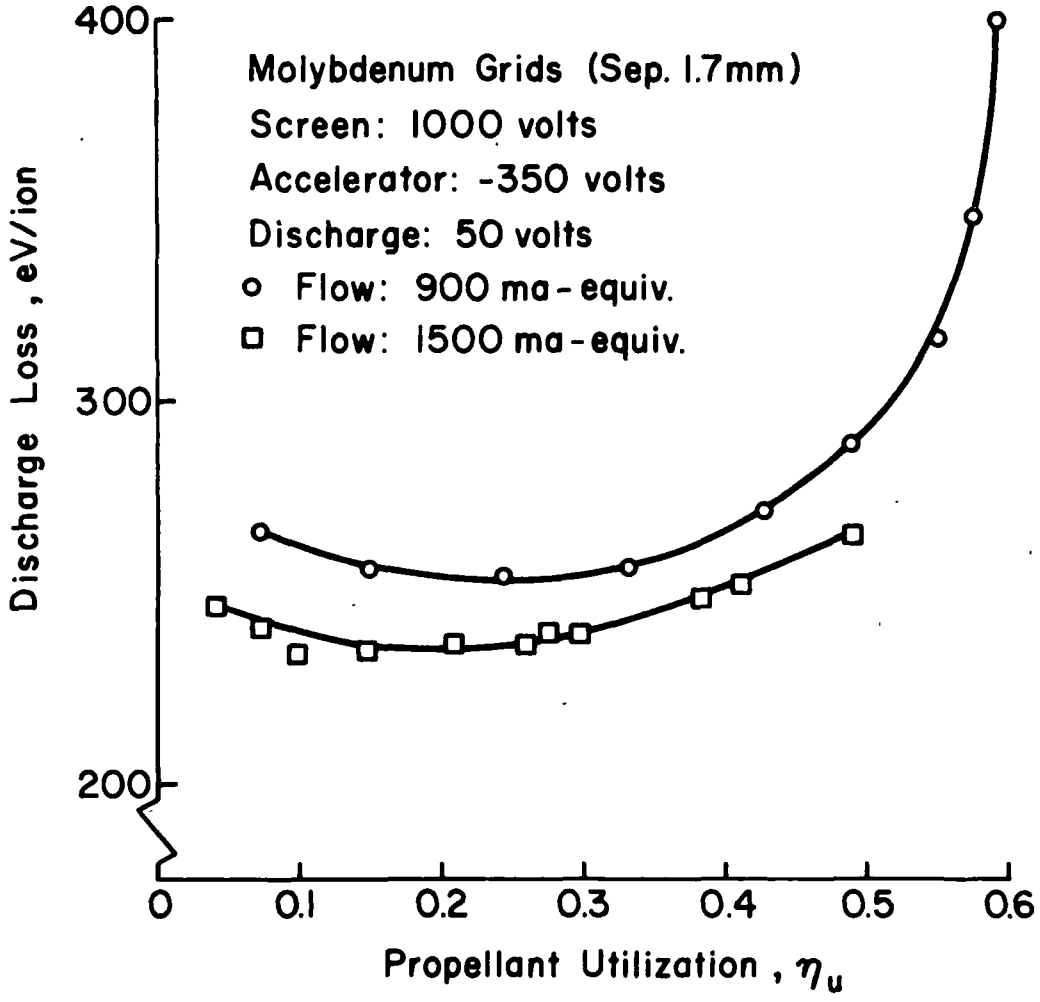

Figure 14. Discharge loss for two different flow rates.

1500 ma-equiv. At the operating conditions of Fig. 14, the maximum beam current obtained was about 200 ma greater at 1500 ma-equiv. flow than at 900 ma-equiv.

For a fixed propellant flow rate and fixed discharge conditions, increasing the total accelerating voltage will tend to increase the extracted beam current and, consequently, the propellant utilization. Because the discharge current and voltage are constant, the discharge loss per extracted ion will also decrease. An increased extraction voltage thus leads to discharge performance curves with generally lower discharge losses and higher utilizations. These trends are shown in Fig. 15 for a range of total extraction voltage from 600 to 1500 volts. Figure 16 shows the same trends for a decreased grid separation (decreased by half). Also the net-to-total voltage ratio has been kept constant at 0.5. The lines of constant discharge current in Fig. 16 permit easy comparison of the same operating condition at various extraction voltages.

While operating the 30-cm source at the design ion energy of 500 eV, performance data of discharge loss and propellant utilization were obtained for several different values of discharge voltage. Discharge losses consistently fell as the voltage was reduced from 60 volts to 45 volts. These data are shown in Fig. 17. Along with lower discharge losses for the reduced discharge voltages, a reduction in the maximum obtainable beam current can also be seen. Reduced discharge voltages

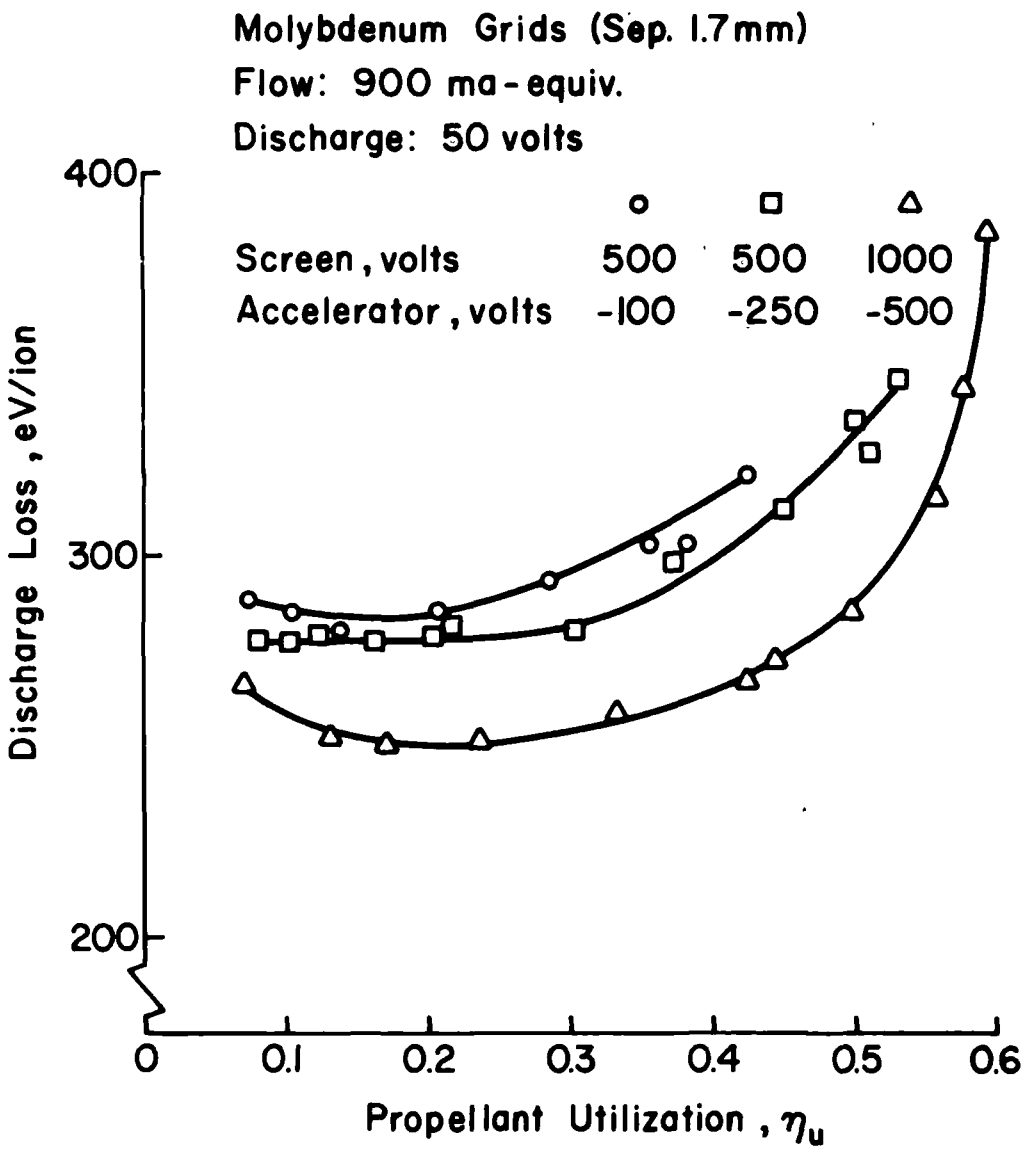

Figure 15. Discharge loss for different total accelerating voltages.

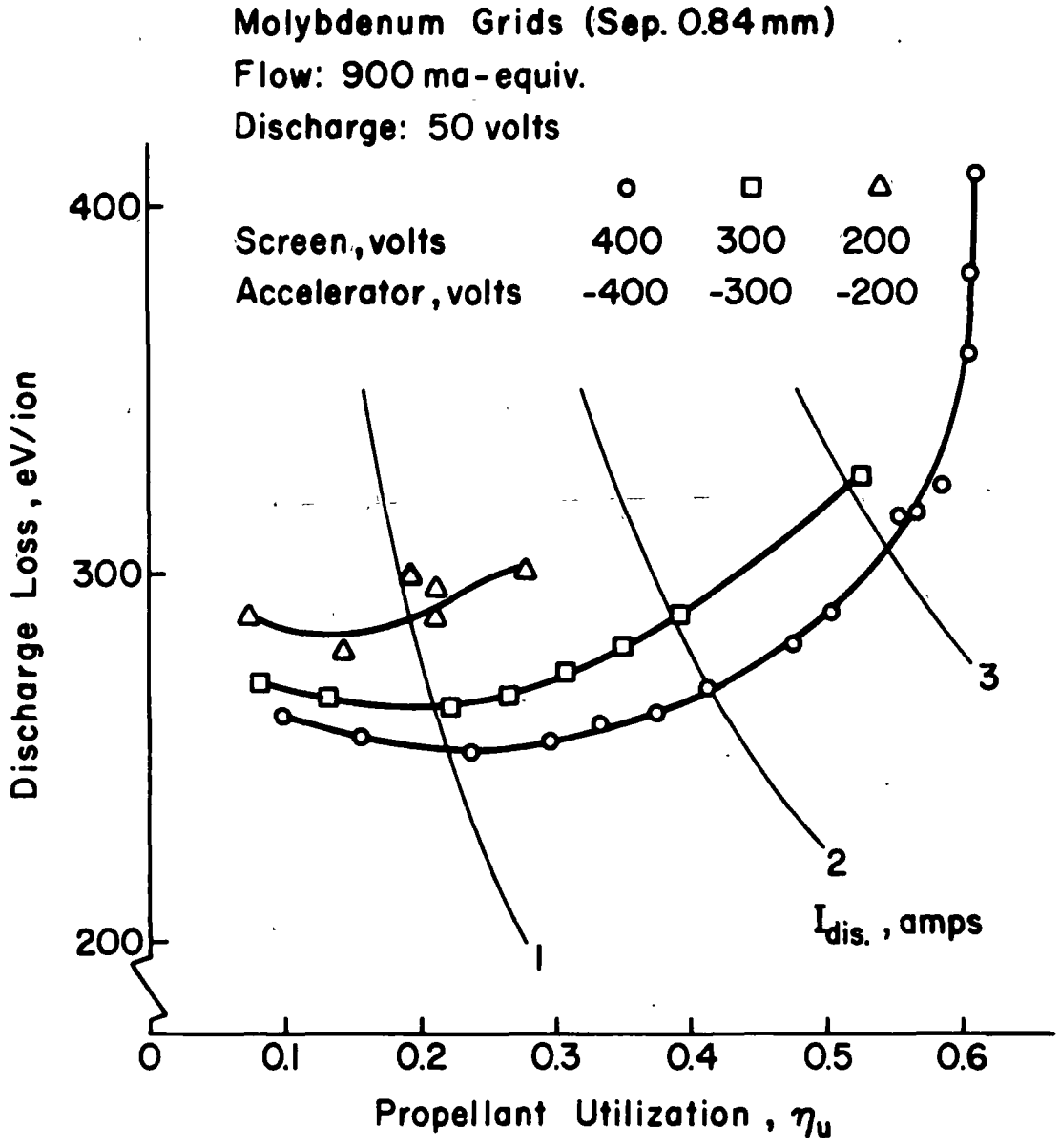

Figure 16. Discharge loss for different total accelerating voltages at the same net to total voltage ratio.

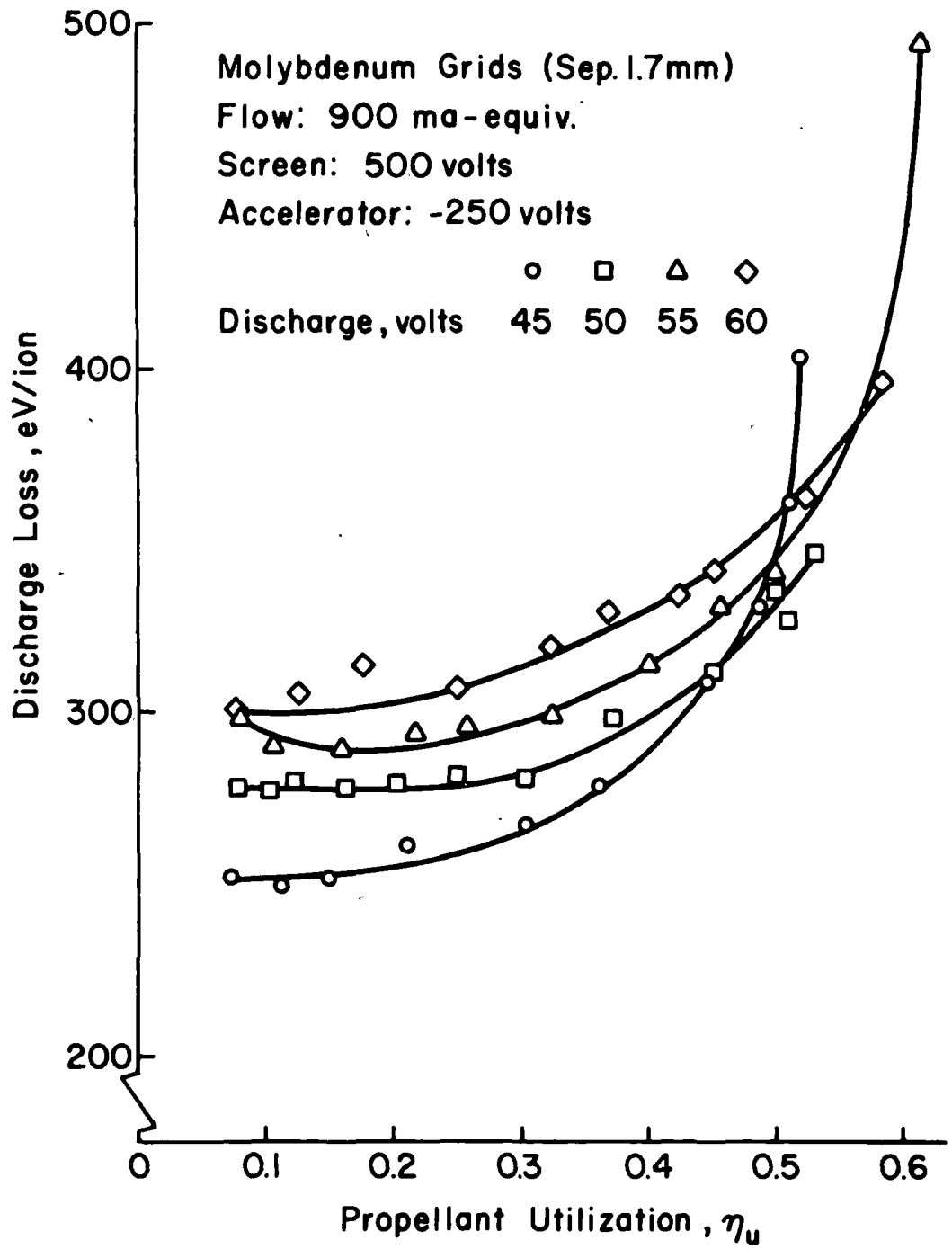

Figure 17. Discharge loss variation with discharge voltage.

tend to reduce the double-ion fraction for the extracted ion beam. The reduced maximum utilization (uncorrected for double ions) may therefore be due in part to reduced double-ion production.

The 30-cm source was operated in a 45-cm bell jar at a number of different facility pressure conditions. Because the propellant was introduced directly into the bell jar system rather than into the source, the concept of propellant utilization has little meaning here. Argon ions could leave the accelerator system, strike a substrate, and return back through the grids as neutrals to be ionized again. Performance data have been plotted as discharge loss versus beam current.

Figure 14 showed the reduction of discharge loss as the propellant flow rate was increased. Figure 18 shows a consistent reduction in discharge loss over a very wide facility pressure range from 2×10^{-5} Torr up to 4×10^{-4} Torr. At the lowest pressures, discharge losses are very high, on the order of 3000 eV/ion. At pressures in the 10^{-4} Torr range, discharge losses approach the levels obtained for operation in the large vacuum facility. The maximum beam current obtained at each pressure was usually limited by the power output of the discharge power supply (about 470 watts).

The effect of increasing the total extraction voltage is again shown in the two bottom curves of Fig. 18. At the same pressure, a higher total voltage reduces discharge losses.

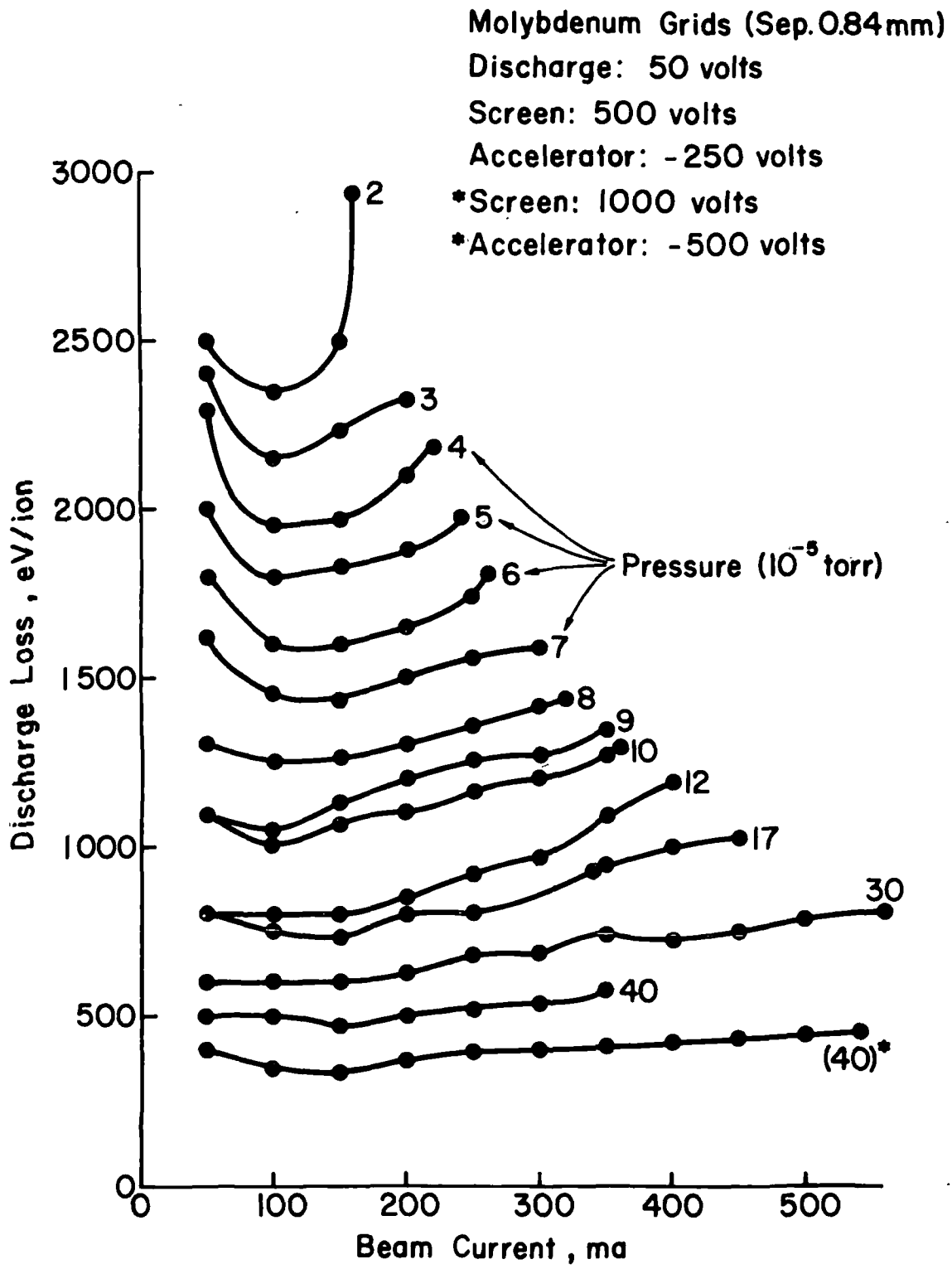

Figure 18. Discharge loss variation with pressure in 45 cm bell jar.

ANODE CONFIGURATIONS

While operating in the large vacuum facility, the 30-cm source was wired so that each of the ten anodes could be individually switched from anode to screen potential. Thus, any combination of anodes could be switched off to observe the effects of anode configuration on source operating characteristics. The anode numbering scheme used in Fig. 6 is retained, with anode #1 as the small center anode at the upstream end and anode #10 closest to the grids.

Switching any single anode,or any pair of anodes, to screen potential changed the beam current extracted but allowed the source to continue operating. Switching off all possible combinations of three anodes allowed the source to continue operating with one exception, when anodes #5, #7 and #9 were switched off together, the discharge was extinguished at both 900 ma-equiv. flow and at 1500 ma-equiv. flow. With only a couple of exceptions turning off almost any four anodes together would extinguish the discharge. Because of the lengthy procedure for initiating the discharge in the large vacuum chamber, it was not possible to check all combinations of four anodes as had been done with all combinations of one, two, or three anodes.

Discharge losses were observed to increase as the number of anodes in operation decreased. If the impedances for

discharge current collection at each anode are effectively in parallel, then the removal of some anodes will increase the overall impedance for discharge current and increase the discharge power dissipated to achieve specific beam current performance conditions.

Figure 19 shows the increase in discharge loss with anodes #1, #2 and #3 off and with anodes #8, #9 and #10 off. The combined length of anodes #8, #9 and #10 is much longer than the combined length of #1, #2, and #3. The discharge loss is seen to be much higher with the three longer anodes off than with the three shorter anodes off.

The only major change in source operating conditions that occurred, as various anodes were turned off, was a decrease in beam current. To illustrate the correlation between these effects, the extracted beam current was plotted as a function of the fraction of total available anode length drawing current. Figure 20 shows reasonable correlation between these two parameters.

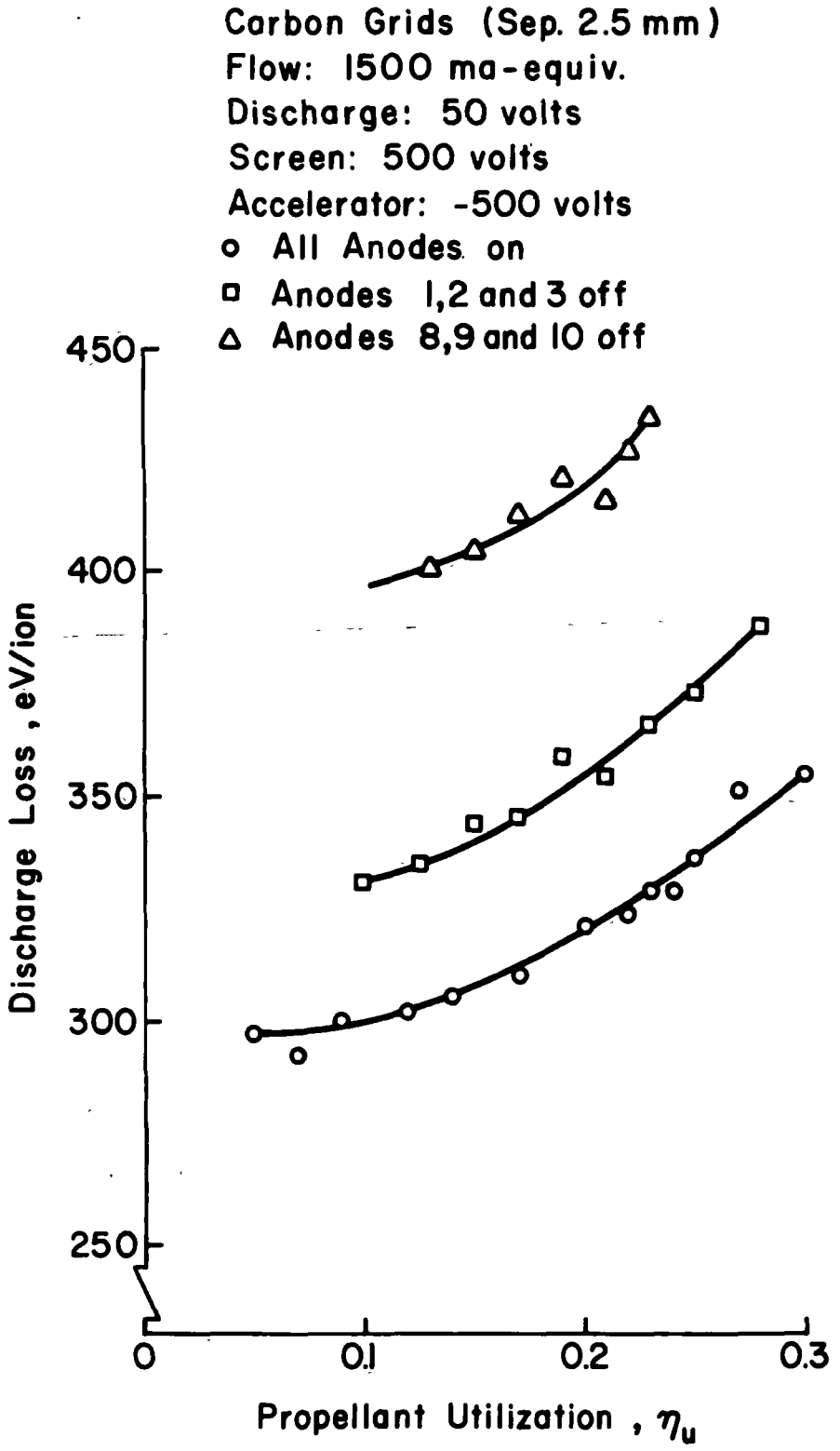

Figure 19. Discharge loss variations with anode configuration.

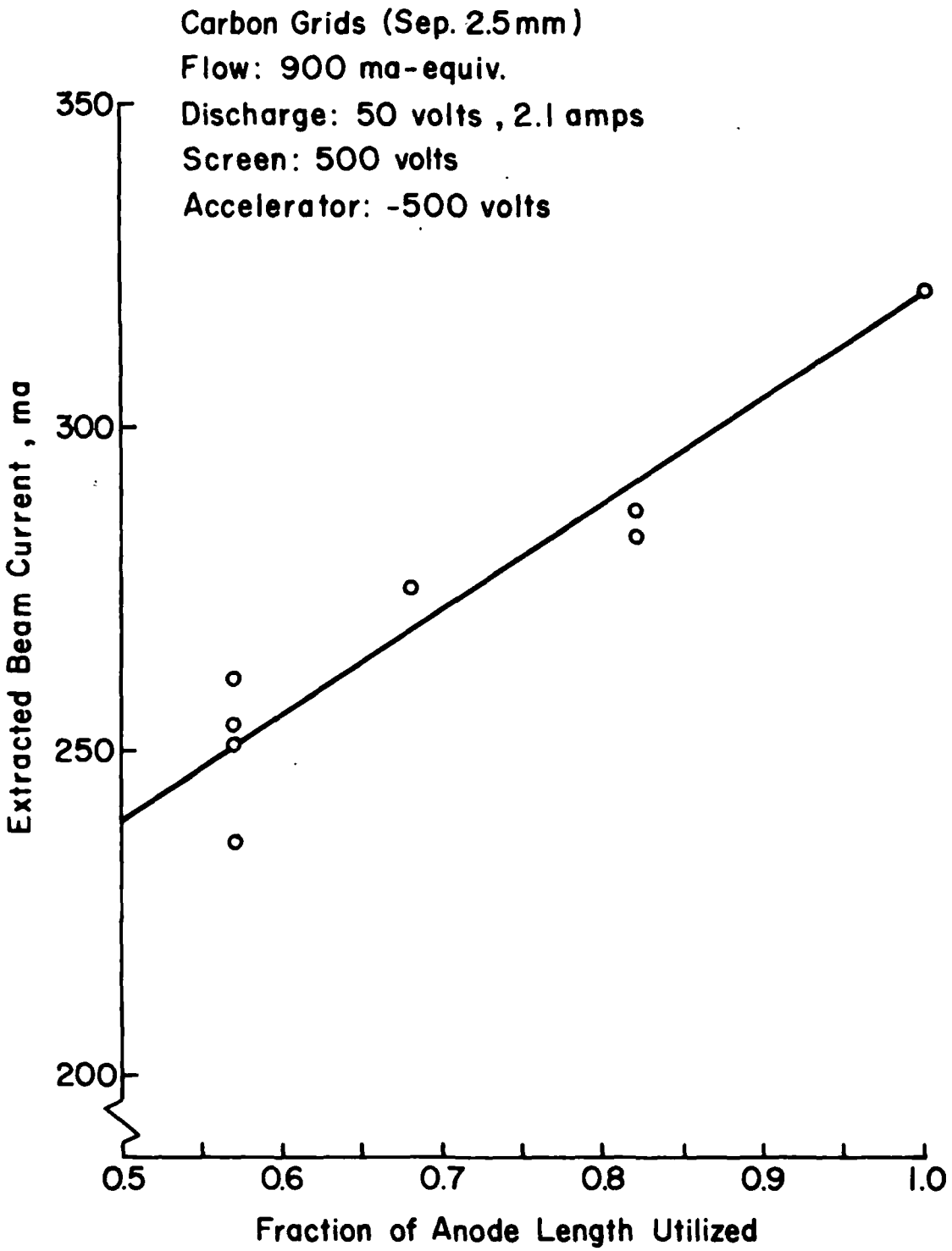

Figure 20. Correlation of extracted beam current with anode configuration.

ION BEAM EXTRACTION

Child's law predicts that the extracted beam current will vary as the 3/2 power of the total extraction voltage maintained between the grids. The beam current extraction characteristics of the molybdenum grids at 1.7 mm separation are shown in Fig. 21, which is a plot of extracted beam current versus total accelerating voltage, with both on logarithmic scales. The slope of a least squares fit line through the data agrees closely with an indicated 3/2 power slope.

The beam currents of Fig. 21 were obtained by increasing discharge power in the ion source until the measured current to the accelerator grid began to deviate sharply from a linear function of beam current. Beam currents were obtained at the operating conditions where the current to the accelerator grid exceeded its linear extrapolation from lower beam currents by 15 percent or, if this limit were not reached, the maximum obtainable beam current was used.

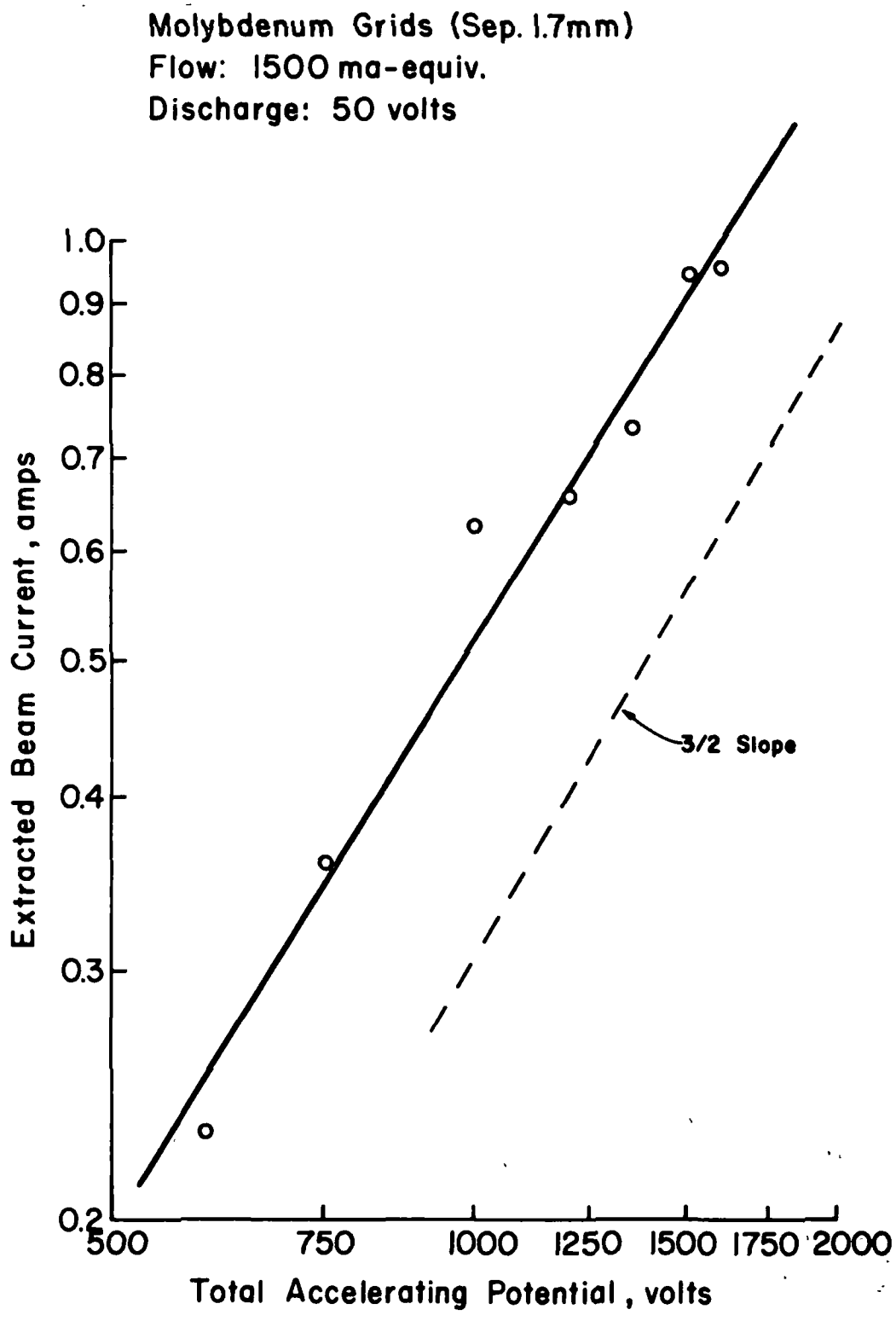

Figure 21. Extracted beam current versus total accelerating voltage for molybdenum grids.

ION BEAM CURRENT PROFILES

The current density in the ion beam was measured with Faraday probes as described in a previous section.

The effect of varying the distance between the probe and the ion source is shown in Fig. 22. The current density in the center of the beam is attenuated about 25 percent as the probe distance is increased from 10 cm to 30 cm. This attenuation is believed to result primarily from ion interactions with the ambient gas in the vacuum facility, together with the local contribution due to neutrals that escape from the ion source. Some attenuation in current density is probably also the result of beam divergence, although beam divergence appears small in the 10 cm to 30 cm range.

Ion beam profiles taken 10 cm from the carbon and molybdenum grids are shown in Figs. 23 and 24 for several combinations of screen and accelerator grid potential. The ion beam current was set for each potential combination by: (1) reaching the maximum beam current for that propellant flow rate; (2) encountering excessive arcing; (3) encountering a rapid increase in impingement with increasing beam current, then decreasing the beam current until the impingement returns to a normal level and stable ion source operation was observed.

There is a difference in the beam profile shape for the two grid sets. The carbon grids gave slightly

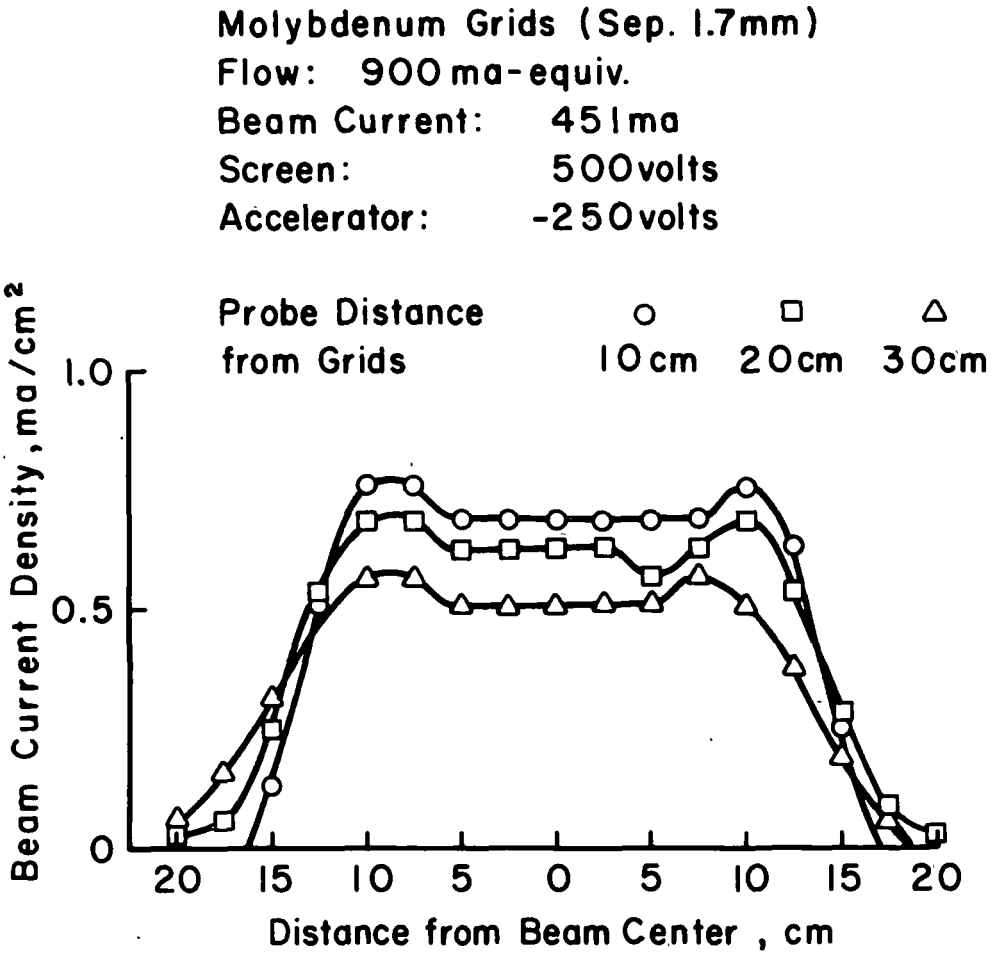

Figure 22. Variation of ion-beam profile with distance from the ion source.

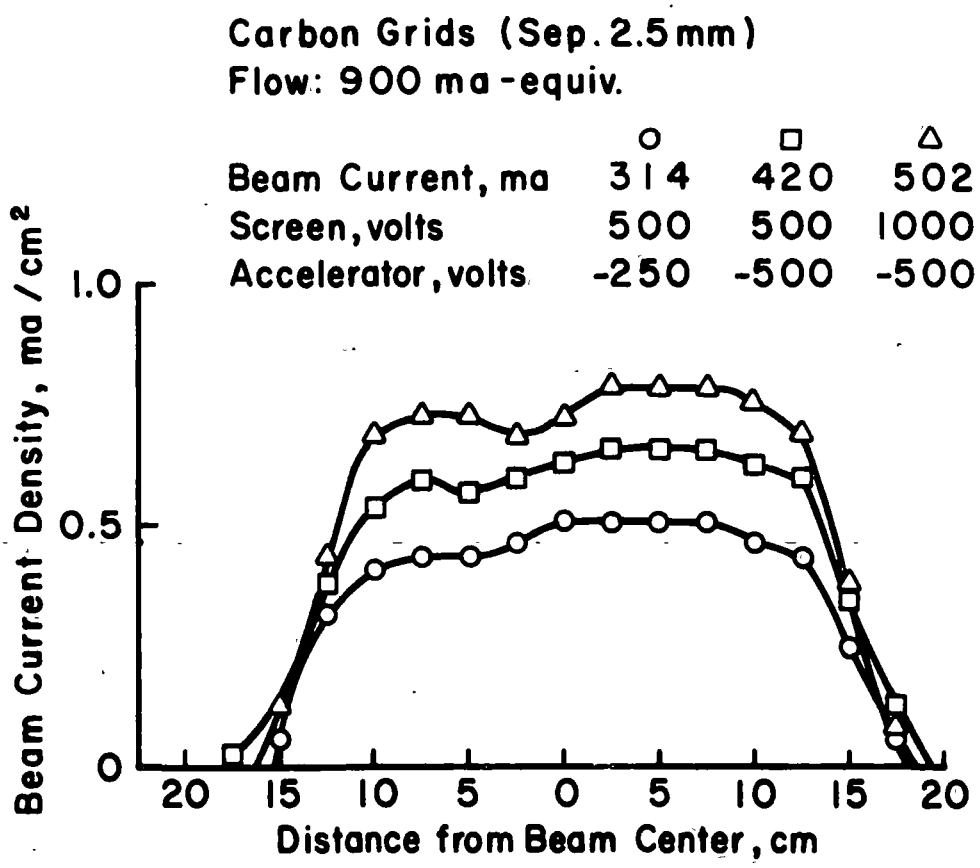

Figure 23. Ion-beam profiles for carbon grids with 900 ma-equivalent argon flow.

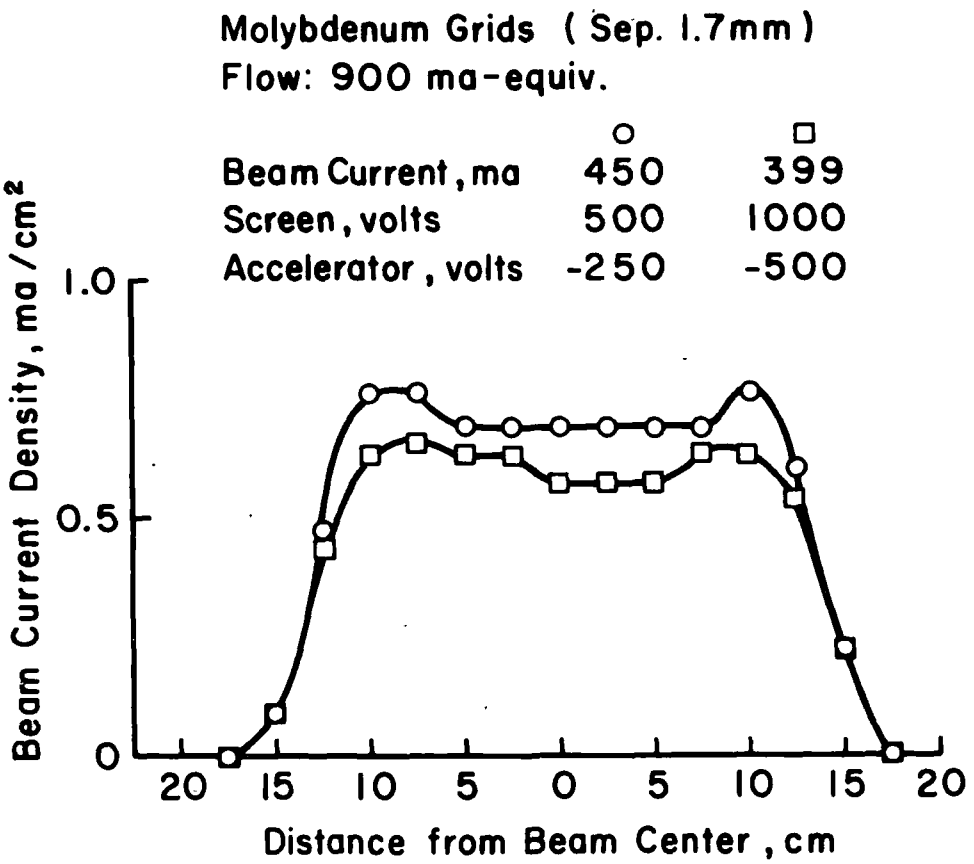

Figure 24. Ion-beam profiles for molybdenum grids with 900 ma-equivalent argon flow.

rounded profiles. The slight asymmetry also shown could be due to a similar asymmetry in either electron emission in the discharge chamber or the gap between the grids. The carbon grids are known to be closer together in the center of the beam, so that the plasma density in the discharge chamber should be slightly more uniform than the profiles shown in Fig. 23.

The profiles for the molybdenum grids are interesting in that they show peaks near the outer edge of the ion beam. If these peaks reflected the variation in discharge-chamber plasma density, then they should have also been evident with carbon grids. The peaks shown in Figs. 22 and 24 are believed to result from the dished shape of the molybdenum grids, although the specifid process is not clear. For example, the spacing between dished grids is known to vary across the beam diameter at operating temperatures.[8] Despite this variation, the relative displacement of screen and accelerator holes to deflect the beamlets in the axial direction was made a linear function of distance from the beam center. This discrepancy would be expected to produce some ion-optic aberration. Another possible cause of the peaks is in the deceleration region downstream of the accelerator. The decelerating electric field is nearly normal to the local dished grid surface, but the ion trajectories are at an appreciable angle to this normal near the edge of the beam. The relative directions of electric field and

trajectories could therefore cause further deflections near the edge of the beam; which could cause the observed peaks.

The maximum current densities in Figs. 23 and 24 differ by only about 10 percent, and are therefore probably determined by the production rate of ions in the discharge chamber. Data were taken at a higher propellant flow rate in an attempt to increase maximum current density. As shown in Fig. 25, a current density of 1 ma/cm^2 was obtained with a flow rate of 1500 ma-equiv. and grid potentials of 500 volts and -500 volts. A substantial increase in total voltage from this 1 ma/cm^2 condition leads to a decrease in beam current, not an increase, because of arcing between the grids at the higher voltages.

Although data for the 1500 mA-equivalent flow rate are not shown for the carbon grids, a current density of about 1.0 ma/cm^2 was obtained at 1000v and -500v. Essentially no improvement was obtained over the 900 mA-equivalent flow at lower voltages.

Figure 26 shows beam current density profiles for molybdenum grids operating in the 45-cm bell jar. The uniformity is as good or better than that obtained in the large vacuum facility. Conspicuously absent are the peaks seen earlier using the molybdenum grids. A significant difference in the configurations is that the grids in the bell jar are not set at the calculated separation for minimum divergence. It is also possible that the signifi-

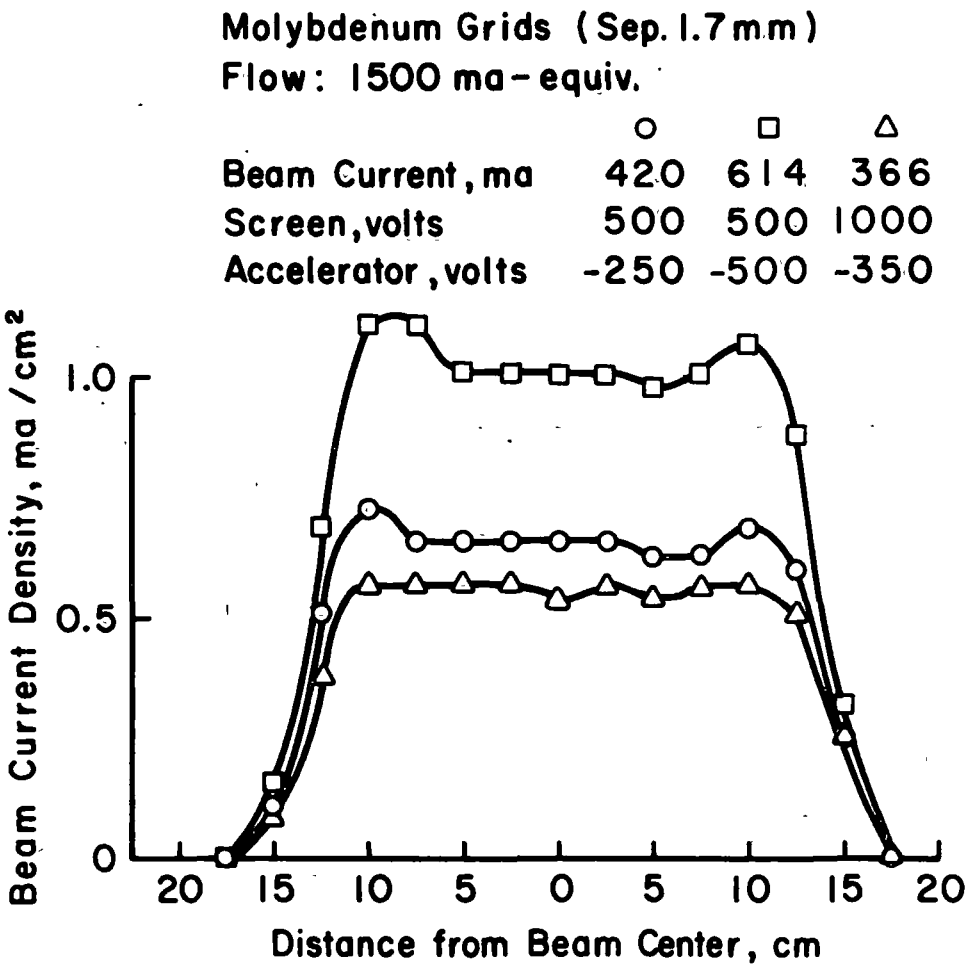

Figure 25. Ion-beam profiles for molybdenum grids with 1500 ma-equivalent argon flow.

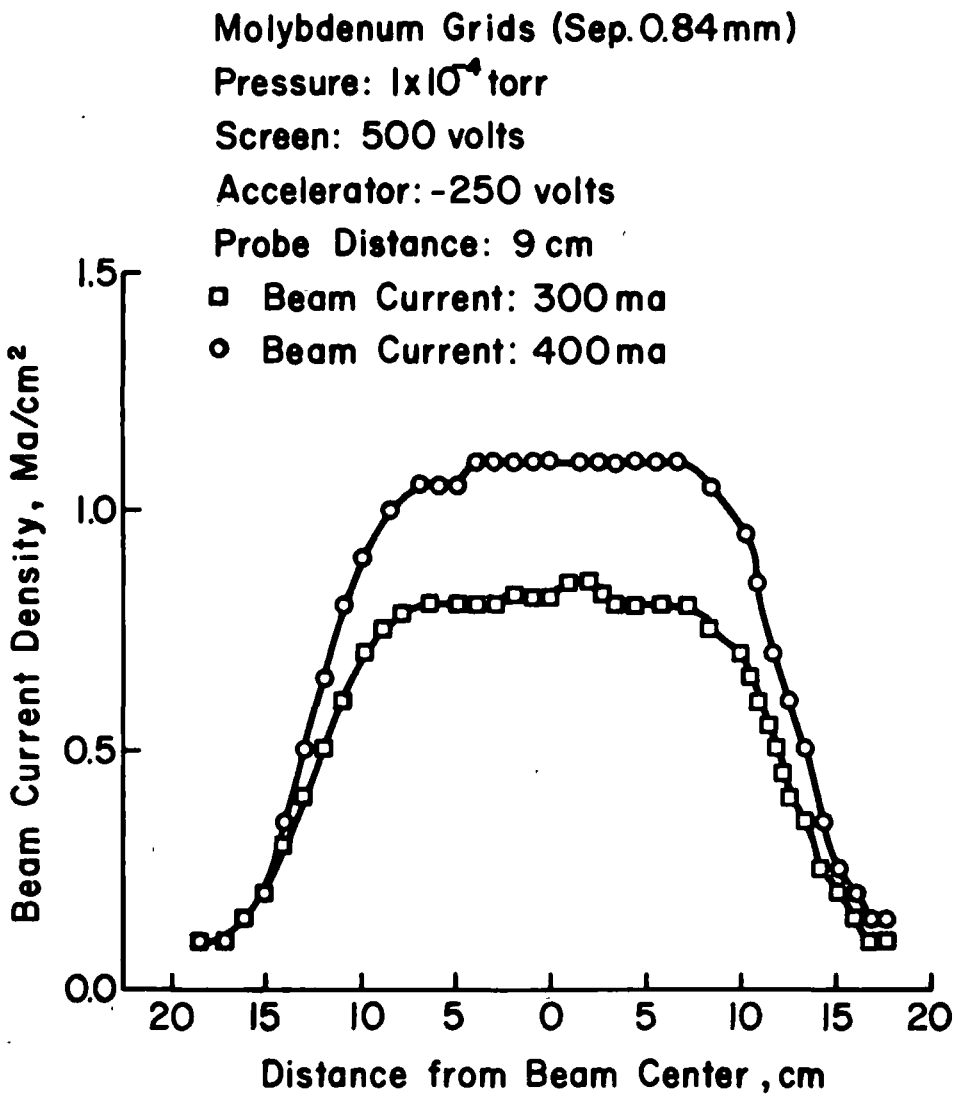

Figure 26. Ion-beam profiles in 45-cm bell jar using molybdenum grids.

cantly higher background pressure causes a greater beam spreading that obscures these peaks. Note that at 9 cm downstream the beam current profile does not approach zero at the edges - unlike the data obtained in the large vacuum chamber.

CONCLUDING REMARKS

The multipole magnetic field used in the 30-cm ion source resulted in low discharge losses and a uniform ion beam. The flat carbon grids permitted current densities up to 1 ma/cm^2, but only at 1000 eV argon ion energy. The dished molybdenum grids permitted the design current density of 1 ma/cm^2 at the design argon ion energy of 500 eV. The difference in performance for these two accelerator systems is attributed, for the most part, to the larger spacing required for the carbon grids.

The uniformity was typically within $\pm$5 percent over the center 20 cm of the beam with the dished molybdenum grids. The uniformity for the flat carbon grids was poorer, averaging $\pm$8 percent for the center 20 cm of the beam.

Of particular interest was the absence of any development iterations in the multipole discharge chamber design. The procedure followed can apparently give a uniform profile and low discharge losses without the usual trial and error development.

PART II

ION BEAM APPLICATIONS

James R. Sites

SOLAR CELLS

Ion beam sputtering was used to fabricate hetero-junction solar cells by depositing indium tin oxide on silicon. These cells have achieved 12 percent conversion efficiency. This technique has proven more successful than thermal evaporation, primarily, we believe, because of the greater process control.

The results, to date, of the solar cell work have been published in Applied Physics Letters (see Appendix A). A second paper, dealing more with the fabrication, (Appendix B) was presented at the 12th IEEE Photovoltaic Specialists Conference, November 15-18, in Baton Rouge and will be published in the proceedings. The follow-up to the solar cell work is now being funded by ERDA.

MIS STRUCTURES

A major difficulty in fabricating high speed integrated circuitry using gallium arsenide and other compound semiconductors has been the formation of insulating barriers between the semiconductor and the metal gate. Such an insulator must be thin (or of high dielectric constant) to give good capacitive coupling, it must exhibit low current leakage, and it must passivate the semiconductor surface to avoid surface states that would pin the Fermi level. The native thermal oxide fulfills these requirements for silicon devices, but not for compound semiconductors at the present time.

Past attempts to form the gallium arsenide insulating barrier through evaporation of an insulator and through anodic oxide growth have been only partially successful. Our technique of sputtering tantalum and silicon oxides onto the gallium arsenide using the ion beam have been at least as successful with much less effort expended so far. The capacitance-voltage and leakage curves for our MIS structures are shown in Figures 1-2.

A paper on the MIS structures has been accepted for presentation at the Physics of Compound Semiconductor Interfaces Conference in Princeton next February with subsequent publication in the Journal of Vacuum Science and Technology. The abstract and summary of results comprise Appendix C.

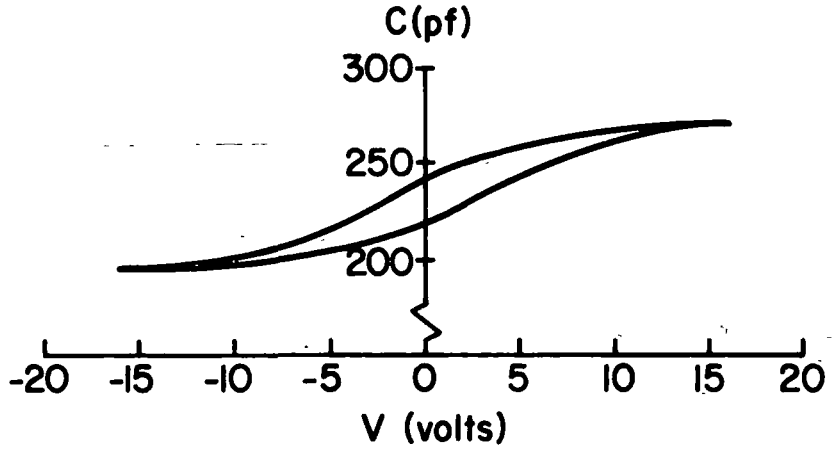

Figure 27. Voltage-capacitance characteristic for Al-SiO_2-GaAs (n-type) capacitor at 300°K (Area: $5.42 \times 10^{-3} cm^2$).

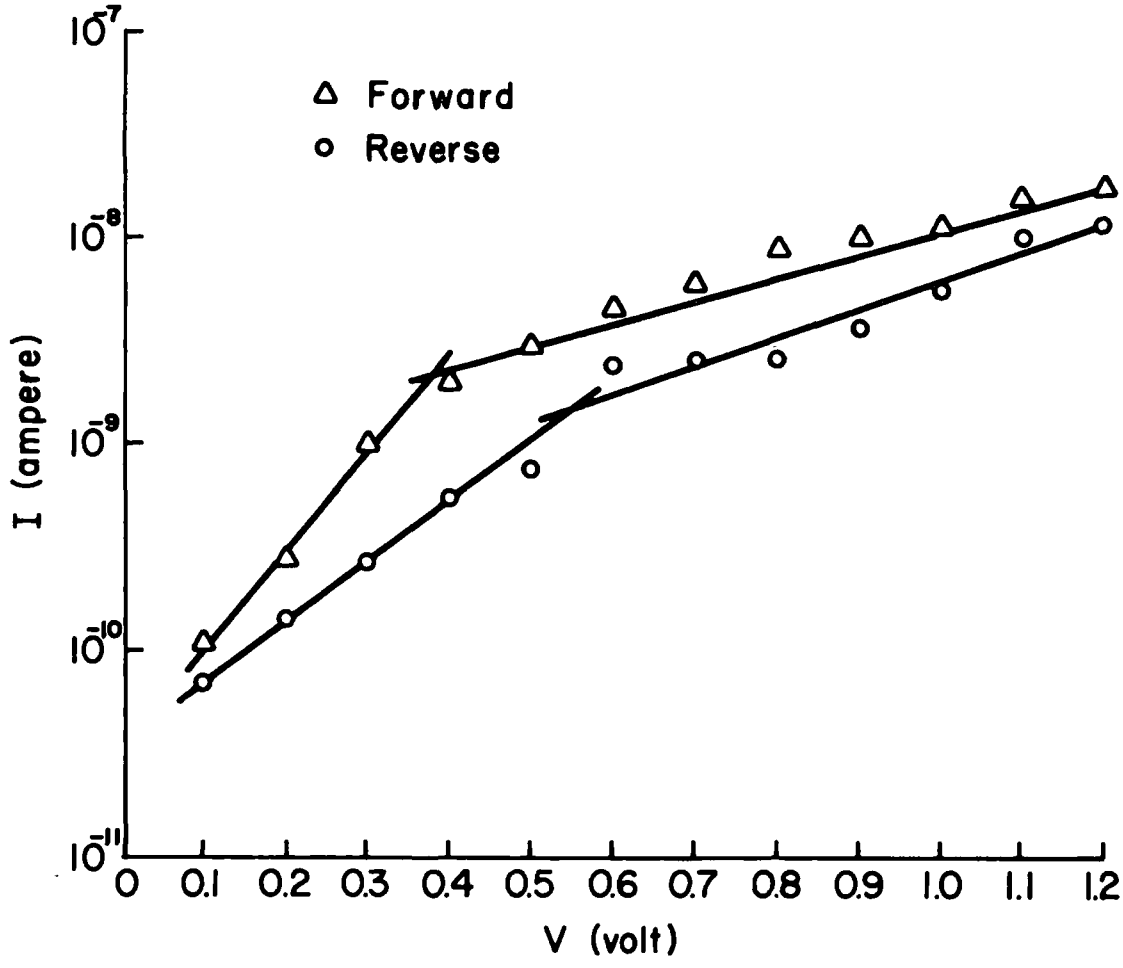

Figure 28. Leakage curves for 1000 Å layer of SiO_2 n-GaAs (Area: $5.42 \times 10^{-3} cm^2$).

Another paper covering semiconductor applications of ion beam sputtering more generally has been submitted to the Metallurgical Coatings Conference of the American Vacuum Society (Appendix D). If accepted, it will be published in Thin Solid Films.

Much of the MIS work is now being funded by the Office of Naval Research.

THINNING AND SURFACE DAMAGE

A series of measurements were made on n-type GaAs samples, which had been milled by a neutralized beam of argon. Gold Schottky barrier contacts were formed on the surfaces of bulk <111> and <100> samples so that the band bending at the surface could be measured before and after milling. Current-voltage measurements on the Schottky diodes indicated that before milling, the barrier height was 1.03 eV, and after milling, the barrier height was 0.48 eV. Capacitance voltage measurements could not be made on the milled samples because the reverse leakage current was too high. A measure of the damage produced by the milling was gained by chemically etching the samples after milling and before depositing the gold Schottky contacts. The depth of the damage was less than 80Å, which was the lower limit of the etch resolution.

Transport measurements of 1 micron thick, n-GaAs epitaxial layers on insulating subatrates indicated that milling produced no measurable changes in the surface conductivity other than the change in thickness. The data do indicate, however, that milling produces a thin (<100 Å) layer at the surface, which has a large number of generation recombination centers.

Eight samples of 1 micron thick, p-type, 30 ohm-cm silicon-on-sapphire were subjected to various surface prepa-

rations, including a standard cleaning procedure, chemical etches in HF solutions, argon-ion milling with 200 eV, 500eV and 800 eV ions, and thermal oxidation treatments. The Hall coefficient and resistivity were measured to determine the net carrier concentration and mobility. The results can be summarized as follows: ion milling, in particular with 500 eV ions, consistently increased the measured mobility from about 70 cm^2/V-sec to about 100 to 130 cm^2/V-sec, while generally decreasing the measured carrier concentration slightly. After chemically etching the surface considerable"ageing" occurred, which was much less pronounced with the ion-milled surfaces. Thermal oxidation after ion milling resulted in mobilities and carrier concentration similar to those prior to milling. Efforts to make C-V measurements on MOS structures were hampered by high series resistance and oxide leakage, and no consistent results were obtained.

REFERENCES

1. N. Laegreid and G. K. Wehner, J. Appl. Phys., Vol. 32, pp. 365-369 (1961).
2. A. L. Southern, W. R. Willis, and M. T. Robinson, J. Appl. Phys., Vol. 34, pp. 153-163 (1963).
3. G. C. Isaacson and H. R. Kaufman, AIAA Paper No. 76-1045 (1976).
4. R. D. Moore, AIAA Paper No. 69-260 (1969).
5. W. D. Ramsey, J. Spacecr. Rockets, Vol. 9, pp. 318-321 (1972).
6. J. R. Beattie and P. J. Wilbur, AIAA Paper No. 76-1011 (1976).
7. G. Aston and H. R. Kaufman, AIAA Paper No. 76-1029 (1976).
8. V. K. Rawlin, B. A. Banks, and D. C. Byers, J. Spacecr. Rockets, Vol. 10, pp. 29-35 (1973).

APPENDIX A

Efficient photovoltaic heterojunctions of indium tin oxides on silicon*

J. B. DuBow and D. E. Burk†

Department of Electrical Engineering, Colorado State University, Fort Collins, Colorado 80523

J. R. Sites

Department of Physics, Colorado State University, Fort Collins, Colorado 80523

(Received 17 June 1976; in final form 5 August 1976)

Heterojunction diodes of indium tin oxide films sputtered onto *p*-silicon using ion beam techniques display significant photovoltaic effects when exposed to sunlight. Galvanomagnetic and optical measurments confirm that the oxide films are highly degenerate transparent semiconductors. At a tin oxide concentration of 10%, we observed an open-circuit voltage of 0.51 V, short-circuit current of 32 mA/cm², fill factor of 0.70, and conversion efficiency of 12%. As the concentration was raised to 70%, the voltage remained steady, the current fell to 27 mA/cm², and the fill factor fell to 0.60.

PACS numbers: 84.60.Jt, 73.40.Lq, 73.60.Fw, 72.40.+w

Certian oxide semiconductors (OS) show promise for wide-scale use in electro-optic applications because of their combination of low electrical resistivity, high optical transmissivity, and environmental ruggedness. Although pure single-crystal indium and tin oxides are insulators, polycrystalline sample exhibit high *n*-type conductivity believed to be caused by oxygen vacancies and substitutional impurities.[1] In this regard, tin oxide is regarded as a donorlike impurity in indium oxide.[2] When deposited upon silicon, indium and tin oxides form good photovoltaic cells. To date, Anderson *et al.* have reported 6% energy conversion efficiency using In_2O_3 evaporated onto *p*-silicon[3] and 10% with SnO_2 evaporated onto *n*-silicon.[4] We have previously reported 3.3% efficiencies using 90% In_2O_3 – 10% SnO_2 sputtered onto *p*-silicon.[5] Now we report studies covering a wide compositional range of indium tin oxides showing energy conversion efficiencies as high as 12% of light close to the sun's spectral distribution. Indium and indium tin oxide devices appear stable, but the stability of the tin oxide cells has yet to be established.

Compared to conventional silicon photovoltaic cells, the oxide semiconductor on silicon (OSOS) structure exhibits the following advantages: (i) The high optical transparency and low electrical resistivity greatly simplify making front contracts. (ii) The oxides exhibit indices of refraction in the right range $(1.9-2.0)^2$ to provide an inherent antireflection coating on silicon. (iii) The effective zero depth junction eliminates any surface dead layer and improves the response at short wavelenths. Moreover, in diffused junction solar cells, as the base doping increases, the dark current and lifetime decrease and the efficiency tends to be lower. In Schottky-type cells, such as those reported here, as the base doping decreases, the dark current decreases, allowing the lifetime, collection depth, radiation resistance, and efficiency to increase. In addition, the ion

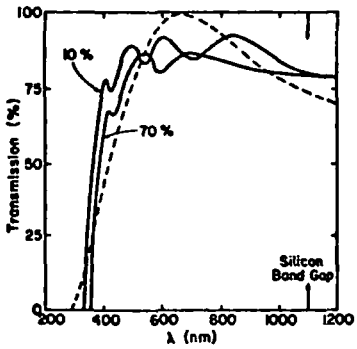

FIG. 1. Optical transmission of 10 and 70% SnO_2 films. Dashed line shows sun's energy spectrum normalized to its maximum value.

beam sputtering technique used to make the diodes is compatible with low-cost continuous fabrication and requires no high-temperature processing.

The starting material was 2-Ω cm single-crystal p-type oxidized silicon. This oxide is used merely to delineate the many 3-mm-diam devices on a wafer and is not an essential fabrication feature. A 5000-Å aluminum layer is evaporated on the back of the wafer for Ohmic contact. An argon ion beam source, supplied by Ion Tech, Inc., was used to sputter clean both the silicon substrate and oxide semiconductor cold-pressed powder target.[6] The oxide semiconductor was then sputtered onto both the silicon wafer and a Corning 7059 glass slide in oxygen partial pressure of 10^{-4} Torr. The primary argon beam energy was 500 eV, and the impingement energy of the sputtered particles ~30 eV. The silicon substrates were maintained at a temperature of 350–400 °C during the deposition, which took approximately 1 h to give the desired 4000-Å film. Photovoltaic cells were made with indium tin oxide compositions ranging from 10 to 70% tin oxide. Contact to the front surface of the cell was made with a gold point probe after fabrication was completed.

Galvanomagnetic and light transmission measurements were made on the glass slides to determine the properties of the indium tin oxide films. Between 77 and 350 °K, the films have a relatively temperature-independent carrier concentration of about 10^{21} cm^{-3} and a mobility of 12 cm^2/V sec. The films exhibit an average visible

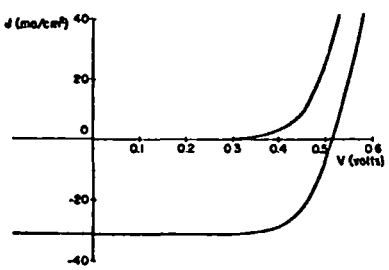

FIG. 2. Current density vs voltage of 90% In_2O_3/10% SnO_2 diode with (lower curve) and without exposure to sunlight.

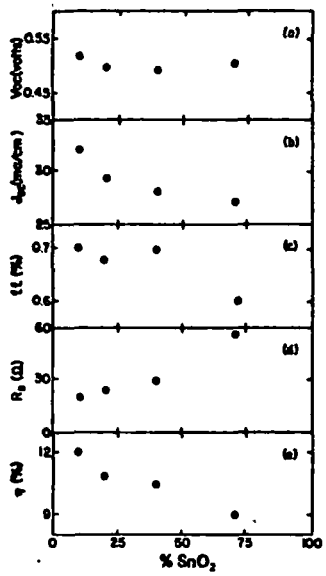

FIG. 3. Compositional variation of photovoltaic parameters; (a) open-circuit voltage, (b) short circuit current density, (c) diode fill factor, (d) series resistance, (e) conversion efficiency in sunlight. Light source: air mass 1.2 sunlight (92 mW/cm^2).

band transmission ranging from 86 to 77% (see Fig. 1), and resistivity of $5-15\times10^{-4}$ Ω cm. For both parameters, the first value quoted is for the 10% tin oxide film, and the second for the 70%. The smaller resistivity could be lowered to 2×10^{-4} by annealing in hydrogen.

Current density–voltage curves for several cells of each composition generally resembled those of Fig. 2 for the 90% In_2O_3 – 10% SnO_2 target. This particular composition displays a 0.70 fill factor, but one that is reduced slightly by the 20-Ω series resistance of the device. The diode quality factor n is approximately 1.5. Illumination translates the diode J-V curves downward with no observable change in the shape for the intensities we used (corresponding to sunlight through 1.2 air masses). Furthermore, the curves showed no large run-to-run differences once we established a substrate temperature during sputtering in the 350–400 °C range mentioned above. The major difference in the curves was the series resistance which varied by as much as 50% within a given composition. The deduced series resistance values were consistent with the resistivity of the film on glass described above.

When the ratio of indium to tin oxide was varied [Fig. 3(a)], we saw very little change in open-circuit voltage, suggesting that the heterojunction barrier is nearly independent of composition. Additional evidence for the relatively weak compositional dependence of the barrier comes from extrapolated C-V measurements, which consistently suggest a voltage intercept of 1.0 ± 0.1 V. This $\frac{1}{2}$-V excess over the open-circuit voltage agrees with the calculations of Peckarer *et al.*[7] Continuing with Fig. 3, we find that both the photocurrent and the diode fill factor fall with increasing tin oxide concentration.

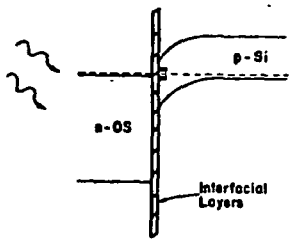

FIG. 4. Suggested band structure of indium tin oxide/silicon heterojunction.

We believe that the smaller current reflects the decrease in optical transmission shown in Fig. 1. The net transmission for the 10% tin oxide film, weighted by the sun's spectrum, is 0.86, whereas for the 70% film it is 0.77. The decrease in fill factor is directly related to the higher series resistance [Fig. 3(d)] in the tin-rich oxides. Although it is not certain that the trends in Fig. 3 are inherent to the indium tin oxide system, they do persist over a variety of fabrication procedures. Since the short-circuit current approaches the theoretical maximum for silicon cells, interfacial recombination is not reducing the photocurrent significantly for any of our compositions. If we take the maximum values from Figs. 3(a)–3(c), which are the true values uncorrected for reflection or other losses, we find a potential power generation of 11 mW/cm^2 for the light we were using (92 mW/cm^2 intensity), corresponding to a conversion efficiency of 12%.

We also find that the oxide semiconductor films adhere well to silicon and glass and are extremely abrasion resistant. The 90% In_2O_3 devices have remained stable over a year's time. A clue to the stability of indium tin oxide cells comes from chemical free energies of formation[8] which are – 207 and – 124 kcal/mole for In_2O_3 and SnO_2, respectively. By comparison, the free energy of formation for SiO_2 is – 193 kcal/mole. Thus, In_2O_3- and indium-rich oxides may be expected to be stable on a silicon substrate, but SnO_2 may very well give up oxygen to the silicon.

Based upon our galvanomagnetic and optical measurements, the oxide films are highly degenerate but transparent semiconductors. The conduction process is essentially temperature independent. Because of the high carrier concentration of the oxide, the entire depletion region lies in the silicon. Photocurrent measurements also demonstrate that electrons flow from the silicon to the oxide. This evidence points to a p-type Schottky barrier model for the photovoltaic cell, as discussed by Anderson,[9] which may be represented by the band structure shown in Fig. 4. The barrier height is relatively constant with composition, indicating that the Fermi level is pinned at the interface. However, the interfacial region is not well characterized and can complicate detailed device modeling. The sputter deposition process, despite its low energy, can cause a shallow damage layer in the silicon.[10] The initial few layers of the deposited film, because of nucleation and lattice accommodation, may not be completely stoichiometric. Moreover, since the sputtering was performed in an oxygen environment on a heated substrate, there is quite likely a thin SiO_2 layer between the oxide semiconductor and the silicon. This insulating layer points to a MIS model for the cell which would affect analysis of the experimental results.[9,11,12] We conclude that heterojunction diodes of indium tin oxides on silicon, particularly those rich in indium oxide, behave like Schottky barrier diodes, display photovoltaic conversion efficiency up to 12%, and have several technical and potential economic advantages for commerical utilization.

We would like to thank Norman Chang for the construction of vacuum chamber fixturing and substrate holder, Peter Tallman for assistance with data collection, Harold Kaufman for advice concerning ion beam techniques, Lawrence Hadley with help in the optical measurements, and Hewlett Packard Company, Loveland, for supplying the oxidized silicon wafers.

*Supported in part by CSU Grant 13-0828 and NASA Grant NSG-3083.
†Hewlett Packard Fellow.
[1]Z. Jarzebski, *Oxide Semiconductors* (Pergammon, New York, 1973).
[2]J.L. Vossen, Phys. Thin Films (to be published).
[3]S.W. Lai, S.L. Franz, G. Kent, R.L. Anderson, J.K. Clifton, and J.V. Masi, 11th IEEE Photovoltaics Specialists Conf. Proc., p. 398 (1975).
[4]R L. Anderson, NSF/RANN Report AER 74-17631, 1975 (unpublished).
[5]J.B. DuBow, D.E. Burk, and J.R. Sites, IEEE Intl. Electron Device Mtg. Tech. Dig., p. 230 (1975).
[6]For more details of the fabrication, see D.E. Burk, J.B. DuBow, and J.R. Sites, 12th IEEE Photovoltaics Specialists Conf. Proc., 1976 (unpublished).
[7]M. Peckarer, H. Lin, and R. Koches, IEEE Intl. Electron Device Mtg. Tech. Dig., p. 213 (1975).
[8]R. Swalin, *Thermodynamics of Solids*, 2nd ed. (Wiley, New York, 1972).
[9]R.L. Anderson, Appl. Phys. Lett. 27, 691 (1975).
[10]H.A. Washburn and J.R. Sites (unpublished).
[11]S.J. Fonash, J. Appl. Phys. 46, 1286 (1975).
[12]R. Singh and J. Shewchun, Appl. Phys. Lett. 28, 512 (1976).

APPENDIX B

FABRICATION OF OSOS CELLS BY NEUTRAL ION BEAM SPUTTERING*

D. E. Burk† and J. B. DuBow

Department of Electrical Engineering

and

J. R. Sites

Department of Physics

Colorado State University

Fort Collins, Colorado, 80523

ABSTRACT

Oxide semiconductor on silicon (OSOS) solar cells have been fabricated from various indium tin oxide $(In_2O_3)_x(SnO_2)_{1-x}$ compositions sputtered onto p-type single crystal silicon substrates with a neutralized argon ion beam. High temperature processing or annealing was not required. The highest efficiency was achieved with $x = 0.91$ and was 12 percent. The cells are environmentally rugged, chemically stable, and show promise for still higher efficiencies. Moreover, the ion beam sputtering fabrication technique is amenable to low cost, continuous processing.

*Supported in part by NASA Grant NSG-3083 and continued under ERDA Contract E(04-3)-1203

†Hewlett-Packard Fellow, Present Address: Wesleyan University, Middleton, CT.

INTRODUCTION

Heterojunction solar cells utilizing transparent oxide semiconductor (OS) films as front layers on silicon wafers have gained recent prominence.[1-4] These cells exploit the high optical transmission and low electrical resistivity of indium oxide, tin oxide, and mixtures of the two.[5,6] The optical transparency allows the bulk of the light to be absorbed in the silicon, while the low resistivity provides a front contact with a manageable series resistance. These materials are wide bandgap (3-4 eV) semiconductors, which as sputtered films tend to be n-type and highly degenerate. They form Schottky barrier-like structures when deposited on p-type (and in some cases n-type) silicon, and they have indices of refraction (1.9-2.0) in the right range to provide an inherent antireflection coating on silicon. Furthermore, they seem to form junctions with silicon which do not exhibit excessive recombination, and hence allow relatively efficient photovoltaic conversion.

Since the OS films are utilized in polycrystalline form, there are distinct simplifications and possibly economic savings in the fabrication procedure. Anderson et. al.[1,2] have deposited indium oxide and tin oxide films by evaporation, while we have chosen to use neutral ion beam sputtering.[3,4] Details of these fabrication procedures and the results achieved to data are reported here.

FABRICATION

Ion Beam Sputtering

The major fabrication step is depositing the oxide semiconductor film onto a silicon wafer. An ion beam sputtering technique is utilized in which a neutralized argon beam strikes a cold pressed powder target, sputtering the material onto a silicon substrate. (See Fig. 1). This type of deposition

offers several economic and technical advantages for solar cell fabrication:

1) No high temperature processing is required. The temperature of both the target and the substrate during sputtering is in the range of 200 - 400°C.
2) The energy of the ion beam is in the proper range to maximize the ratio of target mass removed to total energy input; the energy of sputtered atoms impinging on the substrate is low enough (<30 eV) to diminish concern for surface damage or resputtering.
3) Targets require no special preparation. The composition of binary or ternary oxides may be readily and systematically varied since new targets are easily fabricated.
4) Source and substrate temperatures, system pressure, sputter rate, and beam energy can all be independently varied, allowing many options for process optimization. Reproducible deposition rates are assured once the system is calibrated for a particular material.
5) The ion beam may also be used to sputter clean the substrate surface prior to deposition without breaking the vacuum.
6) The ion beam can be readily scaled up in size to accomodate large scale production.

The ion source used, supplied by Ion-Tech, Inc., produces a 10 cm beam with energy variable from 200-1000 eV, current density up to 2 mA/cm^2, and uniformity better than 10%. The theory of operation for this source, as well as details of its construction, are found in Ref. 7. For the solar cell fabrication, we generally operated the source at 500 eV and 1.5 mA/cm^2, yielding a 4000 Å film in approximately one hour's time.

Sputtering targets are prepared by cold pressing powder mixtures of the desired proportions of indium and tin oxide. (See Fig. 2). The press apparatus

consists of a hydraulic truck jack mounted in an appropriate framework. This arrangement supplies 1000 p.s.i. to the 10 cm diameter targets currently being used. When completed, the targets are relatively sturdy, supported by the aluminum backing plate shown. They have withstood repeated cycling between atmospheric pressure and vacuum and over a several hundred degree temperature range.

Silicon substrates are mounted on a rotatable holder, as are slides of Corning 7059 glass for test films. (See Fig. 3). The substrate holder is equipped with a heater and thermocouple temperature sensor. In the deposition position (Fig. 1, position C) the target and substrate angles have been adjusted to minimize the sputtered particle path length, yet provide nearly uniform coverage.

In practice we find that the best solar cells are made by having a partial oxygen pressure of about 10^{-4} torr in the bell jar, and by heating the silicon substrate to 350-400°C during deposition. Insofar as possible, the oxygen is introduced at the substrate holder. Films deposited under other conditions were generally inferior either electrically or optically, and yield correspondingly poorer devices. Post-deposition annealing improved the poorer solar cells, but had little effect on the better ones.

Summary of Processing

Silicon wafers, both n- and p-type with 2 Ω-cm resistivity, were oxidized on the top surface. The purpose of the oxide is simply to delineate small cells for testing, and it is not an integral part of the processing. The lower surface was metallized at this point with aluminum to provide a back contact when the devices are completed and to insure good thermal contact to the substrate holder during deposition.

The wafers are next attached to the substrate holder behind a thin stain-

less steel mask with 3 mm holes to define the solar cell area. The system is evacuated. With the substrate holder in position A (Fig. 1), the ion beam is activated and used to sputter clean the target. Then the holder is moved to position B, and the oxide that is exposed through the mask is etched away as well as a small amount of the silicon. Finally in position C, the oxygen is introduced and actual deposition takes place as described above. The final configuration is shown in Fig. 4.

The completed cells were generally evaluated without further processing. Electrical measurements were made with a gold tipped prober to contact the front surface at a single point. When post deposition anneals were made, the wafer was scribed and broken to separate the cells into two or more groups.

RESULTS

Deposited Films

The oxide semiconductor films consistently demonstrated very good adherence to both silicon and glass and demonstrated extremely good abrasion resistance, typical of films deposited by ion beam sputtering.[8] Fig. 5 shows the Auger profile of a completed solar cell. The fall off of the indium, tin and oxygen at approximately the same depth, coupled to the apparent lack of interdiffusion of materials from one side of the junction to the other, is consistent with metallurgically abrupt junction.

Electrically the films showed room temperature resistivities of 5-15 x 10^{-4} Ω cm, paralleling the compositional dependence of series resistance (Table 1). The smaller resistivity could be lowered to 2 x 10^{-4} by hydrogen annealing. The carrier concentration and mobility of the films were ∿ 10^{21} cm^{-3} and 12 cm^2/V sec respectively with no appreciable temperature dependence between 77 at 350°K.

Optically the films demonstrated a good transmission of light (see Table I and Fig. 1, Ref. 4). Furthermore, the cell performance characteristics have remained stable over the period of one year since initial fabrication.[4]

Electronics of Cell

Current density vs. voltage curves for the OSOS cells generally resembled those shown in Fig. 6. The direction of electron flow was from the silicon to the oxide semi-conductor. Closer examination shows a diode quality factor of $\sim$ 2.5 at low current densities (below 10^{-4} A/cm^2) and a quality factor $\sim$ 1.5 in the higher current region. This relatively low quality factor, coupled with the magnitude of J_{sc} approaching the theoretical maximum, suggest that interfacial recombination is not a major limitation to performance. At still higher current densities the limitation was due to series resistance as may be apparent from Fig. 5. These general features persisted over a temperature range of 200-410°K.

The basic diode parameters for the different In_2O_3-SnO_2 compositions are given in Table 1. The laboratory light source in each case was an IR filtered tungsten lamp whose intensity was adjusted to 92 mW/cm^2, the noon sun intensity in Fort Collins during the time measurements were made. Spot checks showed ~~that~~ no difference between curves measured in sunlight and those in the laboratory There was no significant sample to sample variation on the same wafer. On different runs of the same In_2O_3 to SnO_2 ratio, V_{oc} and J_{sc} showed little change, but the series resistance varied in some cases as much as a factor of two. The temperature dependence of V_{oc} closely paralleled that of silicon p-n junctions, a decrease with increasing temperature.[9] J_{sc} showed very little temperature dependence over the -50 to +100°C range studies.

When the ratio of indium to tin oxide was varied (Table I), very little

Fraction In_2O_3	0.91	0.8	0.6	0.3
V_{oc} [volts]	0.52	0.49	0.49	0.50
J_{sc} [mA/cm^2]	32	29	28	27
Fill Factor	0.70	0.68	0.70	0.60
Series Resistance [Ω]	20	23	30	58
Shunt Resistance [Ω]	10^5	-	-	-
Average Film Transmission	0.86	-	-	0.77
Maximum Power (mW/cm^2)	11.6	9.7	9.6	9.1
Efficiency	12	10	10	9

Table 1. Summary of solar cell performance parameters. Values are averages of cells on successful fabrication runs.

change in open-circuit voltage was observed, suggesting that the heterojunction barrier is nearly independent of composition. Additional evidence for the relatively weak compositional dependence of the barrier comes from extrapolated C-V measurements, which consistently exhibit a voltage intercept of 1.0 ± 0.1 V. This ½-volt excess over the open-circuit voltage agrees with the calculations of Peckarer et al.[11]

The decrease in photocurrent with increasing SnO_2 concentration parallels the decrease in optical transmission, while the decrease in fill factor seems to correlate with the increased series resistance.

Suggested Device Model

The band structure for the OSOS cells based on the above evidence is shown in Fig. 7. The very high, temperature independent carrier concentration of the oxide semiconductor film makes it degenerate and hence contains a depletion layer of negligible thickness. Electronically, this structure is essentially a p-type Schottky barrier as discussed in Refs. 2 and 4.

The interfacial region is not well characterized at present and likely affects the details of the electronic properties. It may contain some combination of sputter damage at the surface of the silicon, the reformation of a thin SiO_2 layer between cleaning and deposition, or non-stoichiometry in the first layer of the oxide semiconductor. These possibilities point to an MIS-type band structure as discussed by Fonash[11] and Shewchun.[12]

CONCLUSIONS

OSOS heterojunction cells form stable, well-behaved solar cells which have demonstrated up to 12% efficiency. Furthermore, the neutral ion beam sputtering technique is relatively simple and potentially inexpensive. The

basic diode characteristics of the OSOS cells resemble those of silicon p-n junction cells, but the detailed considerations suggest a Schottky barrier or MIS structure.

ACKNOWLEDGMENTS

Several people have helped with this project. We are grateful to Norman Chang for help with bell jar fixturing and temperature dependent measurements, to Harold Kaufman for ion beam advice, to Lawrence Hadley for optics advice, to Ronald Kee for Auger Profiles, to Peter Tallman for measurement assistance, and to Hewlett Packard Co. for the oxidized wafers.

REFERENCES

1. S. W. Lai, S. L. Franz, G. Kent, R. L. Anderson, J. K. Clifton, and J. V. Masi, 11th IEEE Photovoltaics Specialists Conf. Proc., p. 398 (1975).

2. R. L. Anderson, Appl. Phys. Lett. 27, 691 (1975).

3. J. B. DuBow, D. E. Burk, and J. R. Sites, IEEE Intl. Electron Device Mtg. Tech. Dig., p. 230 (1975).

4. J. B. DuBow, D. E. Burk, and J. R. Sites, Appl. Phys. Lett. 29, 494 (1976).

5. J. L. Vossen, Phys. Thin Films 9, (1976).

6. Z. Jarzebski, Oxide Semiconductors (Pergammon, New York, 1973).

7. P. D. Reader and H. R. Kaufman, J. Vac. Sci. Technol. 12, 1344 (1976).

8. R. C. Pan, L. C. Meiners, and J. R. Sites, J. Vac. Sci. Technol., to be published.

9. H. J. Hovel, Solar Cells (Academic Press, New York). 1975

10. M. Peckarer, H. Lin, and R. Koches, IEEE Intl. Electron Device Mtg. Tech. Dig., p. 213 (1975).

11. S. J. Fonash, J. Appl. Phys. 46, 1286 (1975).

12. R. Singh and J. Shewchun, Appl. Phys. Lett. 28, 512 (1976).

FIGURE CAPTIONS

Figure 1	Schematic of ion beam sputtering apparatus.
Figure 2	Target preparation.
Figure 3	Substrate holder.
Figure 4	Completed solar cell.
Figure 5	Auger profile of indium tin oxide/silicon solar cell.
Figure 6	Current density vs. voltage for $(In_2O_3)_{.9}(SnO_2)_{.1}$/Si diode in dark (upper) and AM 1.2 sunlight (lower curve).
Figure 7	Suggested band structure of OSOS solar cell.

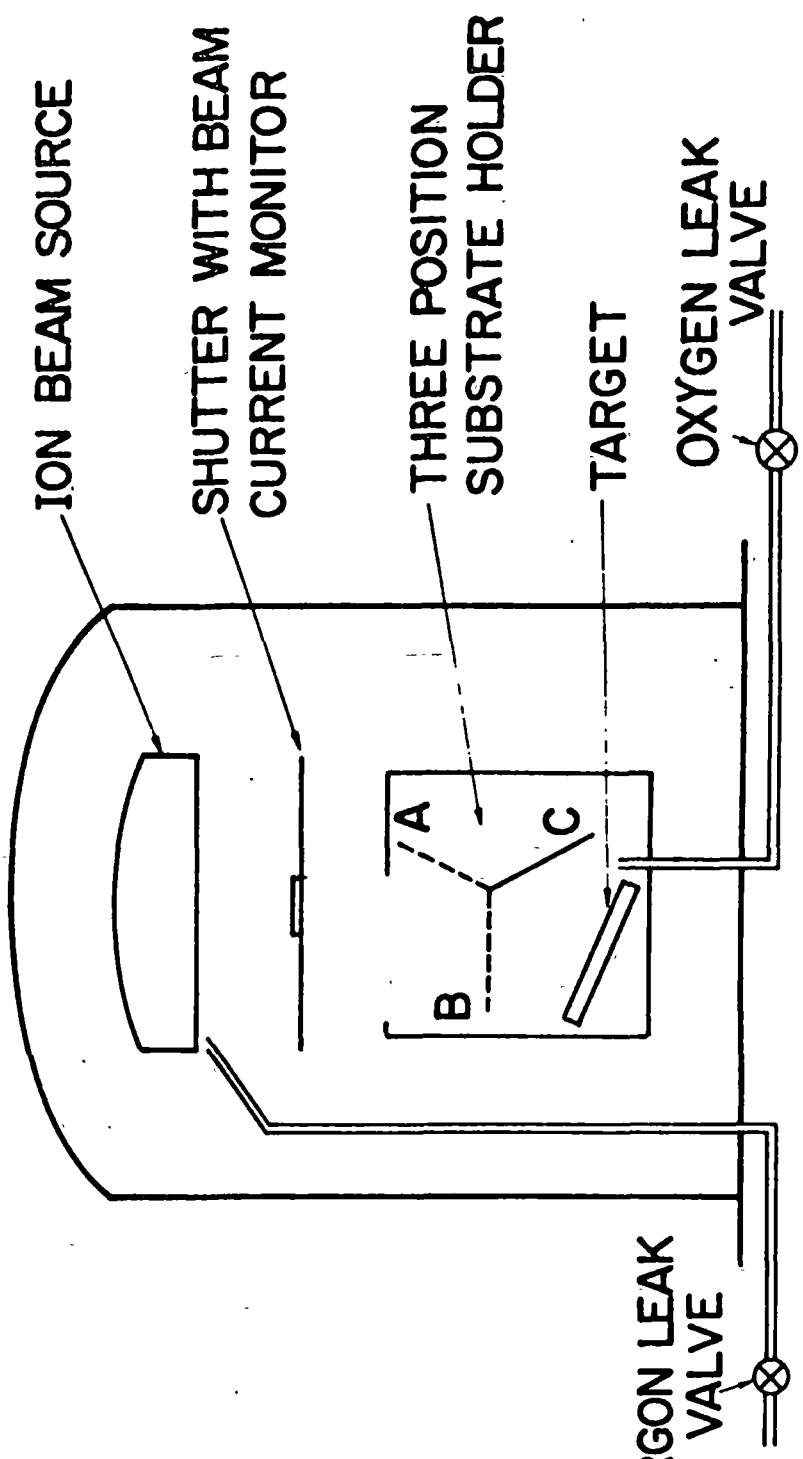
ION BEAM SOURCE
SHUTTER WITH BEAM CURRENT MONITOR
THREE POSITION SUBSTRATE HOLDER
TARGET
OXYGEN LEAK VALVE
ARGON LEAK VALVE
A
B
C

Fig. 1

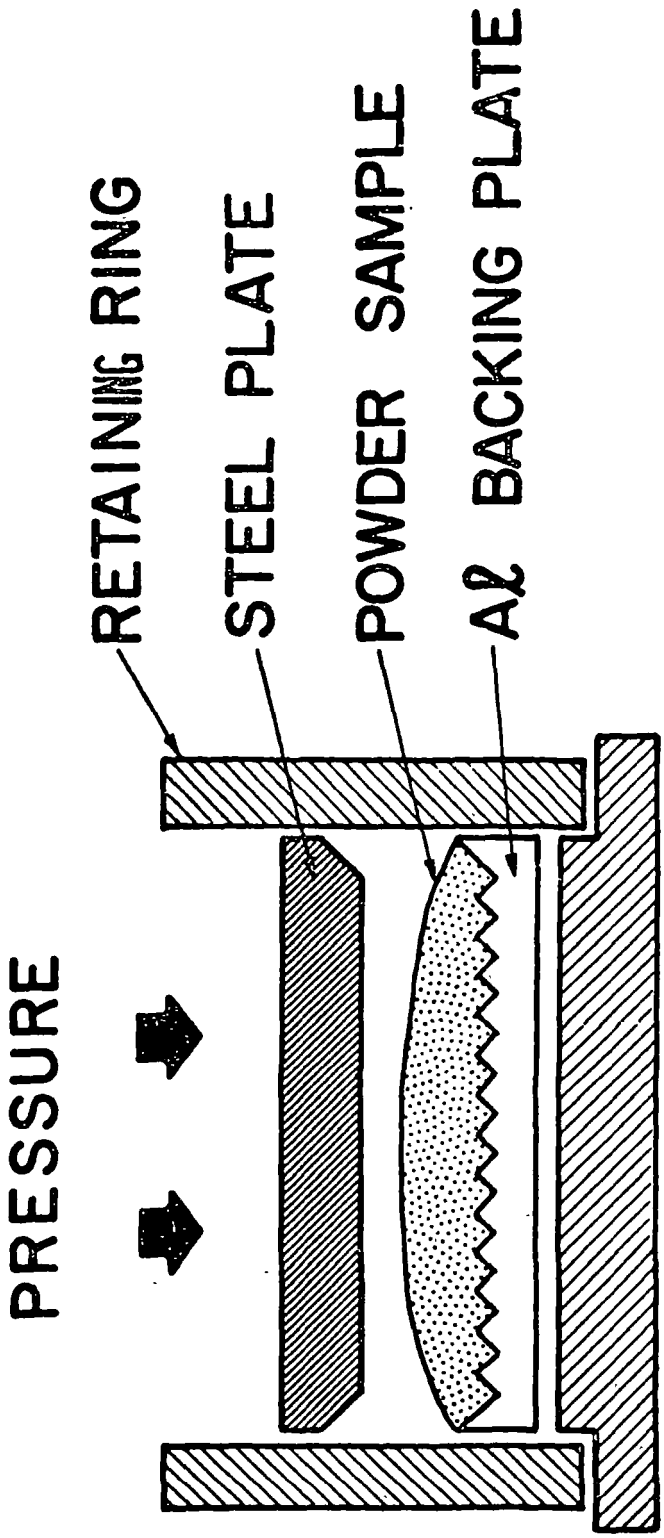
PRESSURE
RETAINING RING
STEEL PLATE
POWDER SAMPLE
Al BACKING PLATE

Fig. 2

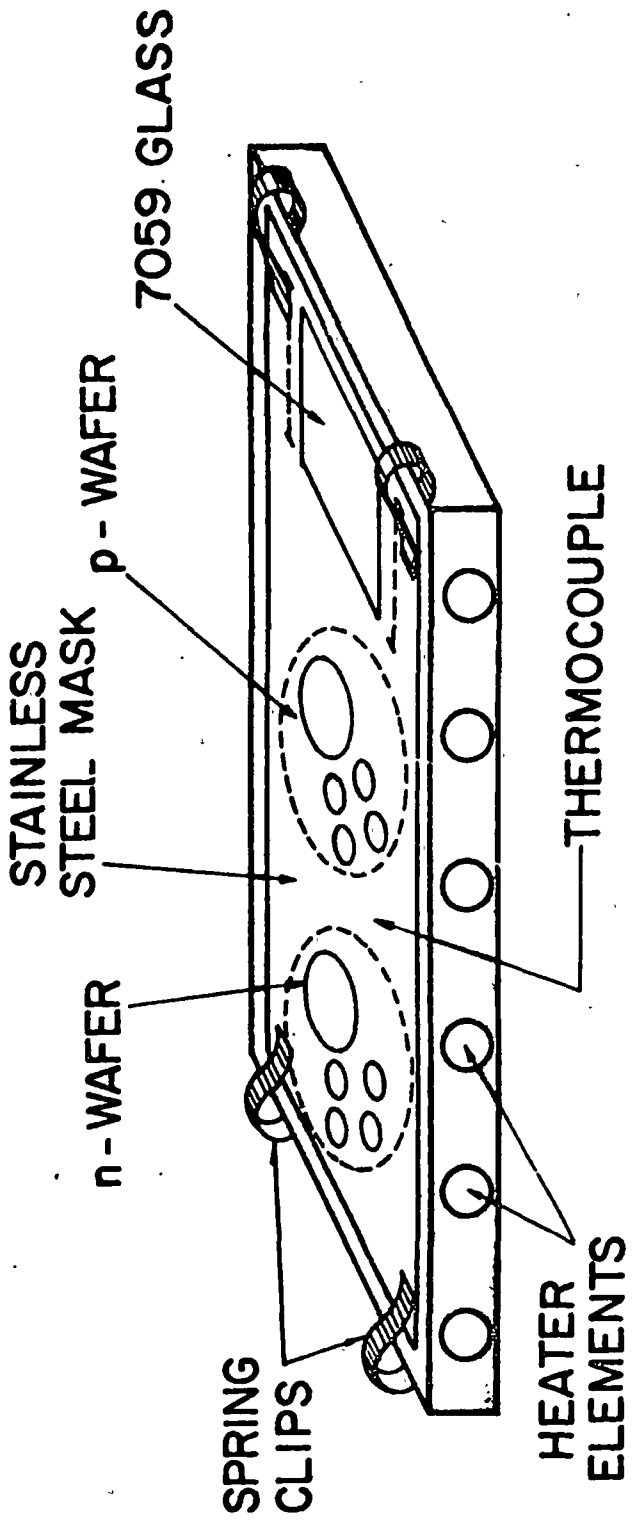
7059 GLASS
p - WAFER
STAINLESS STEEL MASK
n - WAFER
THERMOCOUPLE
SPRING CLIPS
HEATER ELEMENTS

Fig. 3

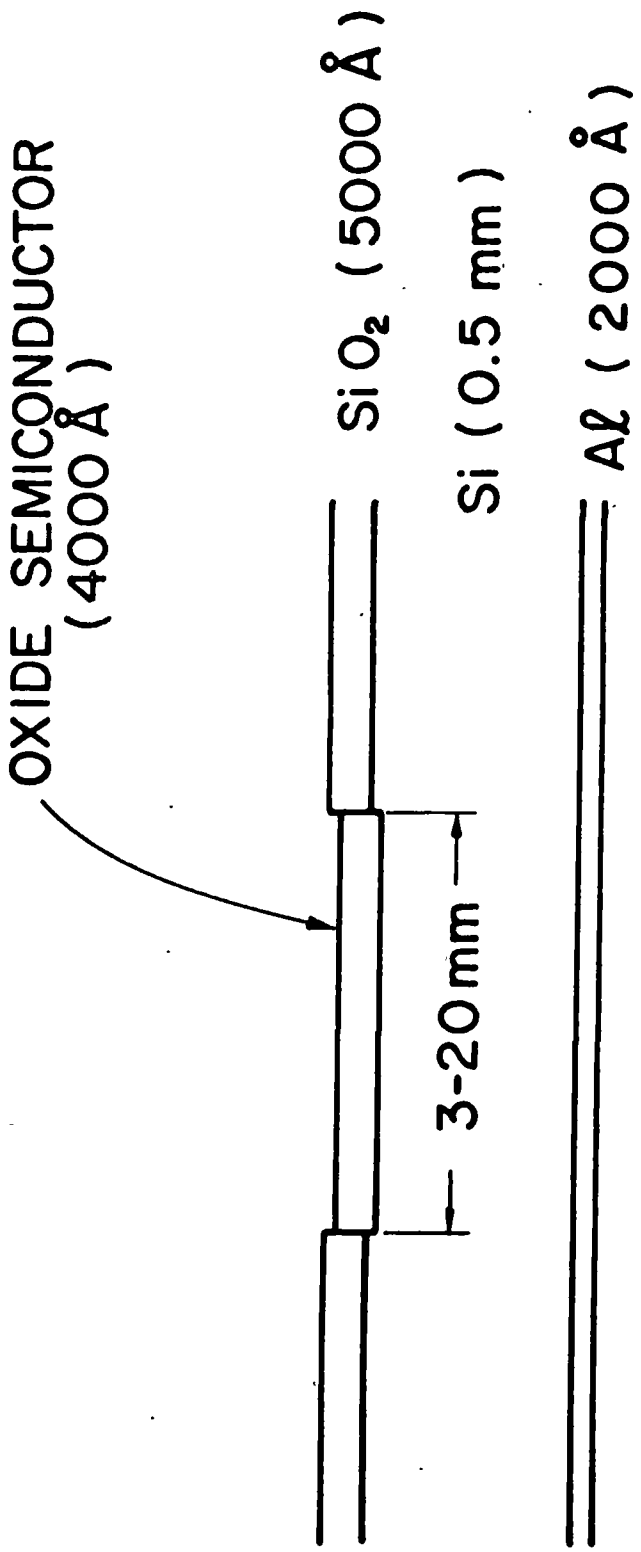
OXIDE SEMICONDUCTOR
(4000 Å)
SiO_2 (5000 Å)
Si (0.5 mm)
Al (2000 Å)
3-20 mm

Fig. 4

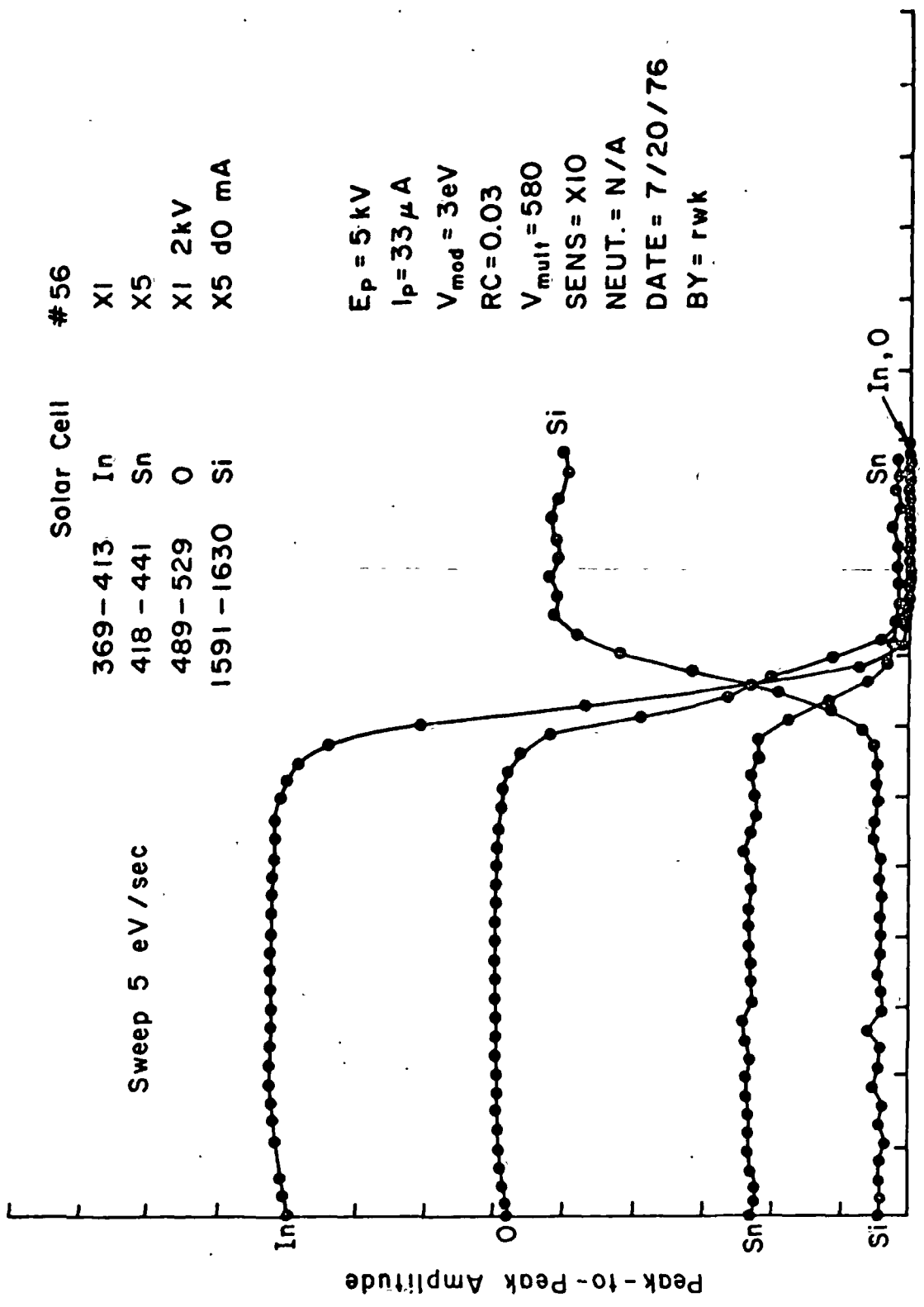
Solar Cell #56
369-413 In X1
418-441 Sn X5
489-529 O X1 2kV
1591-1630 Si X5 d0 mA
Sweep 5 eV/sec
E_p = 5 kV
I_p = 33 μA
V_{mod} = 3eV
RC=0.03
V_{mult} = 580
SENS= X10
NEUT.= N/A
DATE= 7/20/76
BY= rwk
Si
Sn
In,O
In
O
Sn
Si
Peak-to-Peak Amplitude
Time (5 minutes/division)

Fig. 5

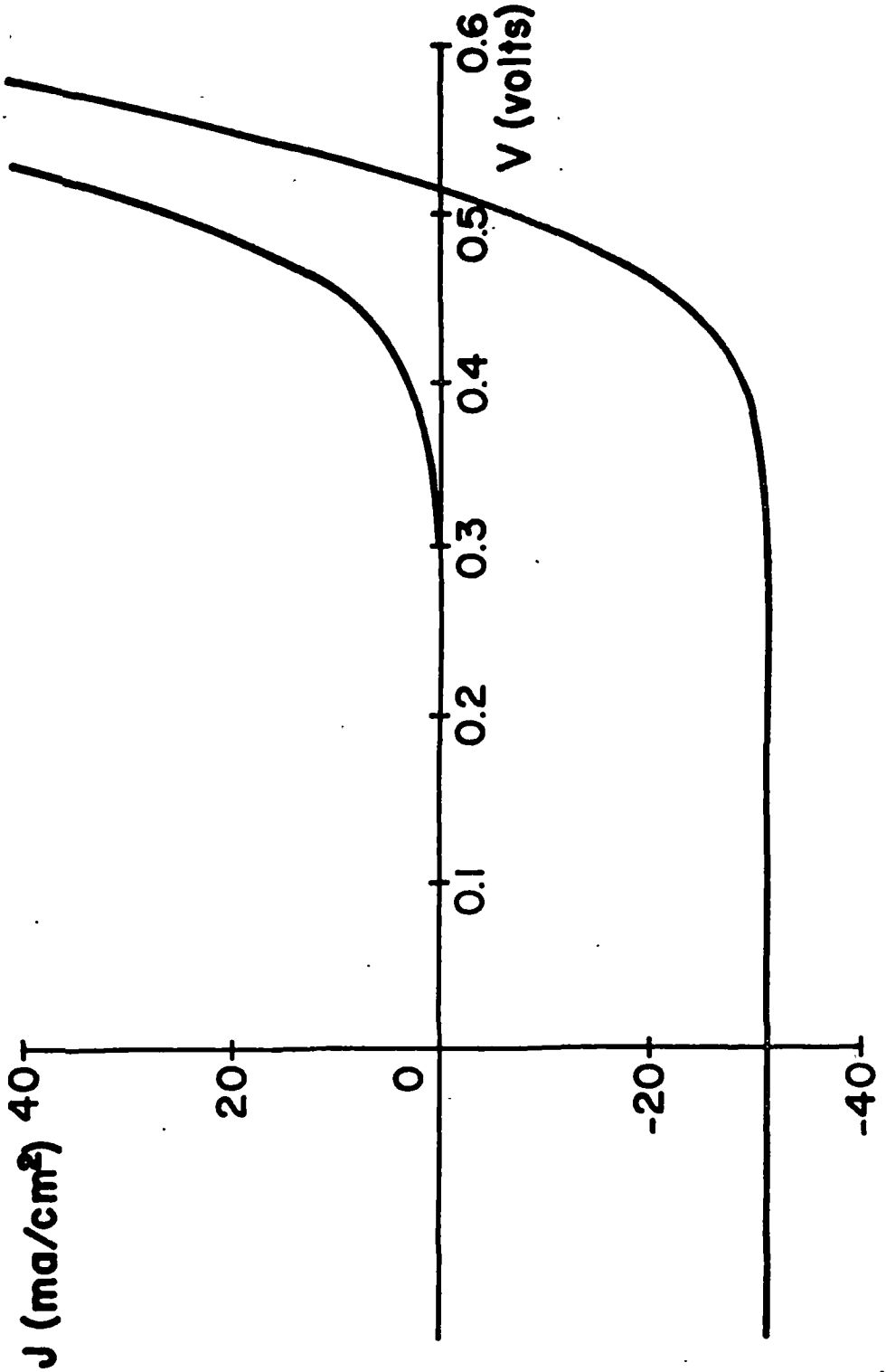

Fig. 6

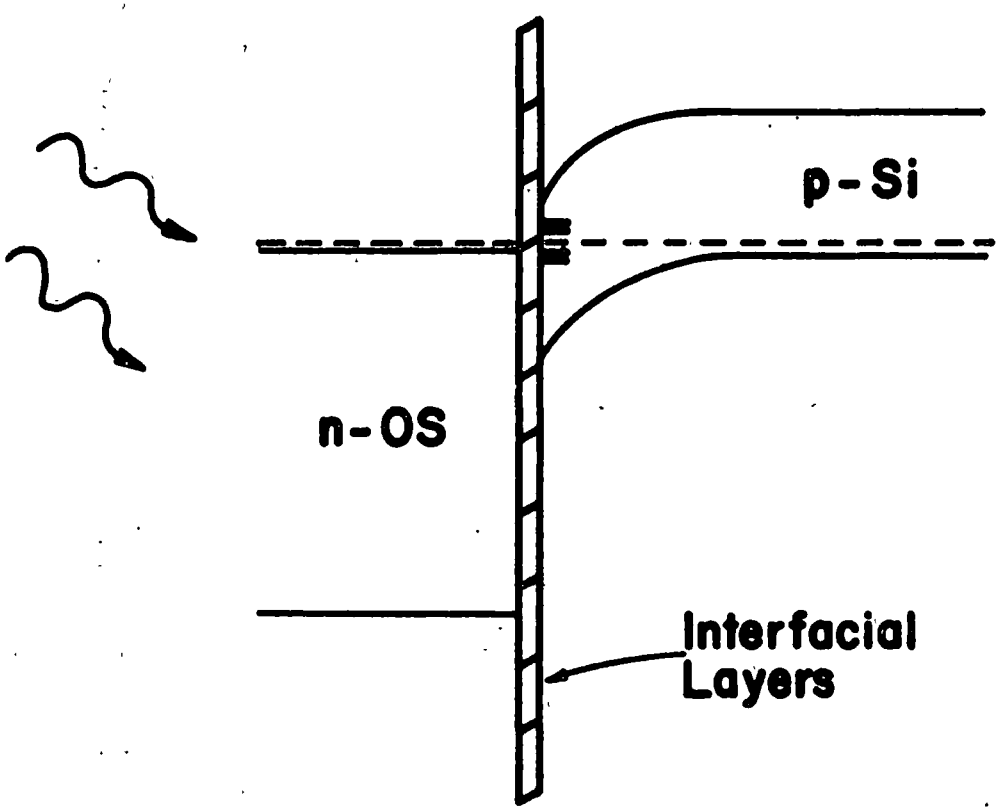

Fig. 7

APPENDIX C

Oxide Barriers on GaAs by Neutral Ion Beam Sputtering*

R. C. Pan, L. G. Meiners†, and J. R. Sites

Physics Department, Colorado State University

Fort Collins, Colorado, 80523

ABSTRACT

Tantalum and silcon oxides have been sputter deposited onto gallium arsenide using a 500 eV beam of neutralized argon atoms. MIS devices had capacitances that could be varied from full accumulation to depletion with the application of modest voltages. Other measurements (breakdown field, dielectric constant, leakage current, adherence, Auger profile, and photoluminescence) also suggest that these structures hold potential usefulness for insulated gate GaAs circuitry.

*Support by NASA and by ONR.

†Permanent Address: Naval Electronics Laboratory Center, San Diego, CA

Oxide Barriers on GaAs by Neutral Ion Beam Sputtering

R. C. Pan, L. G. Meiners, and J. R. Sites

SUMMARY

The problem of preparing an insulating layer on gallium arsenide with interfacial and physical properties suitable for construction of a technologically useful MIS device has not yet been solved. Reactive rf sputtering of silicon oxide and silicon nitride on III-IV semiconductors has produced MIS devices with pinned Fermi levels. Anodic oxides have shown some promise, but still have relatively large slow surface state densities and somewhat poor mechanical properties.

This paper describes the preparation and measurement of sputtered dielectric layers of tantalum and silicon oxides on n-type <100> and <111> gallium arsenide substrates. The sputtering was done with a neutralized beam of low energy (500 eV) argon ions striking tantalum and quartz (SiO_2) targets. This technique has the advantage that the sputtered particles collecting on the substrate are themselves electrically neutral.

The deposited oxides were in the 500-2000 Å thickness range. Bell jar partial pressures were typically 1×10^{-4} torr of oxygen and 3×10^{-4} torr argon. The substrates were not intentionally heated during deposition.

Capacitance - voltage measurements on MIS structures (area ~ 1 mm^2) showed the number of surface charges trapped at the semiconductor-insulator interface under zero applied voltage was 5×10^{11} cm^{-2} for the tantalum oxide layers and 1×10^{12} cm^{-2} for the silicon oxide. When the Fermi level is brought to the band edge these values become 5×10^{12} and 6×10^{12} cm^{-2} respectively.

Breakdown fields for the tantalum and silicon oxides were 2×10^6 and 3×10^6 V/cm. The relative dielectric constants were 18-20 and 4.0, the tantalum

oxide somewhat lower than the 26 reported for Ta_2O_5, but the silicon oxide value the same as SiO_2 within the accuracy of the thickness measurements. Low voltage resistivities were 1×10^{12} and 5×10^{10} Ω-cm respectively with the leakage less than 10 na at full accumulation and depletion.

All of the sputtered layers were extremely adherent and quite scratch resistant. Annealing cycles with both hydrogen and helium consistently degraded the tantalum oxide films. Auger analysis showed no sign of contamination in the dielectric layers, and photoluminescence did not reveal trapping levels at the GaAs surface.

APPENDIX D

SEMICONDUCTOR APPLICATIONS OF THIN FILMS DEPOSITIED BY NEUTRAL ION BEAM SPUTTERING

James R. Sites

Physics Department

Colorado State Universtiy

Fort Collins, Colorado, 80523

ABSTRACT

Thin films deposited by sputtering with a neutralized ion beam source have shown promise for performance improvement in two distinct types of devices: heterojunction solar cells and insulating barriers on gallium arsenide. The source used, first developed by NASA for space propulsion, accelerates positive argon ions to 200-800 eV, and then neutralizes them with an electron discharge. The resultant beam is four inches in diameter, extremely uniform, and has a flux variable up to 2 mA/cm^2. The beam strikes a target not electrically involved in the acceleration, and hence may be an insulator or a powder. The sputtered particles are also electrically neutral, possibly aiding the uniformity and electrical characteristics of the deposited films. Each parameter of the technique is independently controllable, and the films formed have shown very good adhesion and abrasion properties.

Heterojunction solar cells were fabricated by depositing $\sim$ 4000 Å of indium tin oxide $(In_2O_3)_x(SnO_2)_{1-x}$ on single crystal silicon. The concentration was varied over a wide range, yielding the best cells for $x = 0.91$. These cells had an open circuit voltage of 0.51, diode fill factor of 0.70, diode quality factor of 1.5, and conversion efficiency of 12%. The films themselves are both transparent (77-86% transmission) and conductive ($5\text{-}15 \times 10^{-4}$ Ω cm).

Insulating barriers 500-2000 Å thick were deposited on GaAs by the same

sputtering techniques. Tantalum oxide was formed by sputtering from tantalum metal in an oxygen environment, and silicon oxide by sputtering quartz. MIS devices ($\sim$ 1 mm^2) showed capacitances that could be varied from full accumulation to depletion with modest voltage. Surface state densities were in the low 10^{12} cm^{-2} range, breakdown voltages 2-3 x 10^6 V/cm, and leakage currents below 10 nA in the operating voltage range. Dielectric constants were close to those of Ta_2O_5 and SiO_2. Auger and photoluminescence measurements failed to reveal impurities or traps near the dielectric - semiconductor interface.

DISTRIBUTION LIST

	No. of Copies
National Aeronautics and Space Administration Washington, D. C. 20546	
Attn: RPE/Mr. Wayne Hudson	1
Mr. Daniel H. Herman, Code SL	
National Aeronautics and Space Administration Lewis Research Center 21000 Brookpark Road Cleveland, Ohio 44135	
Attn: Research Support Procurement Section	
Mr. Allen Jones, MS 500-313	1
Technology Utilization Office, MS 3-19	1
Report Control Office, MS 5-5	1
Library, MS 60-3	2
N. T. Musial, MS 500-113	1
Spacecraft Technology Division, MS 54-1	
Mr. E. Davison	1
Mr. R. Finke	1
Mr. D. Byers	1
Mr. B. Banks	1
Mr. S. Domitz	1
Mr. F. Terdan	1
Mr. P. Thollot	1
Mr. W. Kerslake	1
Mr. E. Theman	10
Mr. M. Mirtich	1
Physical Science Division, MS 301-1	
Mr. W. E. Moeckel	1
National Aeronautics and Space Administration Marshall Space Flight Center Huntsville, Alabama 35812	
Attn: Mr. Jerry P. Hethcoate	1
Research and Technology Division Wright-Patterson AFB, Ohio 45433	
Attn: (ADTN) Lt. David A. Fromme	1
NASA Scientific and Technical Information Facility P. O. Box 8757 Baltimore/Washington International Airport Baltimore, Maryland 21240	40
Case Western Reserve University 10900 Euclid Avenue Cleveland, Ohio 44106	
Attn: Dr. Eli Reshotko	1

Royal Aircraft Establishment
Space Department
Farnborough, Hants, England
Attn: Dr. D. G. Fearn 1

United Kingdom Atomic Energy Authority
Culham Laboratory
Abingdom, Berkshire, England
Attn: Dr. P. J. Harbour 1
Dr. M. F. A. Harrison 1
Dr. T. S. Green 1

National Aeronautics and Space Administration
Goddard Space Flight Center
Greenbelt, Maryland 20771
Attn: Mr. W. Isley, Code 734 1
Mr. R. Hunter 1
Mr. R. Callens, Code 734 1

SAMSO
Air Force Unit Post Office
Los Angeles, California 90045
Attn: Capt. D. Egan/SYAX 1

Comsat Laboratories
P. O. Box 115
Clarksburg, Maryland 20734
Attn: Mr. B. Free 1
Mr. O. Revesz 1

Rocket Propulsion Laboratory
Edwards AFB, California 93523
Attn: LKDA/Mr. Frank Mead 2

DFVLR - Institut für Plasmadynamik
Technische Universitat Stuttgart
7 Stuttgart-Vaihingen
Allmandstr 124
West Germany
Attn: Dr. G. Krülle 1

DFVLR - Institut für Plasmadynamik
33 Braunschweig
Bienroder Weg 53
West Germany
Attn: Mr. H. Bessling 1

Giessen University
1st Institute of Physics
Giessen, West Germany
Attn: Professor H. W. Loeb 1

Jet Propulsion Laboratory
4800 Oak Grove Drive
Pasadena, California 91102
Attn: Dr. Kenneth Atkins 1
Technical Library 1
Mr. Eugene Pawlik 1
Mr. James Graf 1
Dr. John R. Beattie 1

Electro-Optical Systems, Inc.
300 North Halstead
Pasadena, California 91107
Attn: Mr. R. Worlock 1
Mr. E. James

TRW, Inc.
TRW Systems
One Space Park
Redondo Beach, California 90278
Attn: Mr. M. Huberman 1
Dr. J. M. Sellen 1

National Aeronautics and Space Administration
Ames Research Center
Moffett Field, California 94035
Attn: Technical Library 1

National Aeronautics and Space Administration
Langley Research Center
Langley Field Station
Hampton, Virginia 23365
Attn: Technical Library 1

Hughes Research Laboratories
3011 Malibu Canyon Road
Malibu, California 90265
Attn: Dr. Jay Hyman 1
Mr. J. H. Molitor 1
Mr. T. D. Masek 1
Dr. R. L. Poeschel 1
Mr. R. Vahrenkamp 1

United States Air Force
Office of Scientific Research
Washington, D. C. 20025
Attn: Mr. M. Slawsky 1

Princeton University
Princeton, New Jersey 08540
Attn: Mr. W. F. Von Jaskowsky 1
Dean R. G. Jahn 1
Dr. K. E. Clark 1

Communications Research Centre
Ottawa, Ontario, Canada
Attn: Dr. W. F. Payne 1

Joint Institute for Laboratory Astrophysics
University of Colorado
Boulder, Colorado 80302
Attn: Dr. Gordon H. Dunn 1

Department of Aeronautics and Astronautics
Stanford University
Stanford, California 94305
Attn: Professor Howard S. Seifert 1

Boeing Aerospace Company
P. O1 Box 3999
Seattle, Washington 98124
Attn: Mr. Donald Grim 1

Intelcom Rad Tech
7650 Convoy Court
P. O. Box 80817
San Diego, California 92138
Attn: Dr. David Vroom 1

Lockheed Missiles and Space Company
Sunnyvale, California 94088
Attn: Dr. William L. Owens
Propulsion Systems, Dept. 62-13 1

Fairchild Republic Company
Farmingdale, New York 11735
Attn: Dr. William Guman 1

COMSAT Corporation
950 L'Enfant Plaza SW
Washington, D. C. 20024
Attn: Mr. Sidney O. Metzger 1

Electrotechnical Laboratory
Tahashi Branch
5-4-1 Mukodai-Machi, Tanashi-Shi
Tokyo, Japan
Attn: Dr. Katsuva Nakayama 1

Office of Assistant for Study Support
Kirtland Air Force Base
Albuquerque, New Mexico 87117
Attn: Dr. Calvin W. Thomas OAS Ge 1
Dr. Berhart Eber OAS Ge 1

Bell Laboratories
600 Mountain Avenue
Murray Hill, New Jersey 07974
Attn: Dr. Edward G. Spencer 1
Dr. Paul H. Schmidt 1

Massachusetts Institute of Technology
Lincoln Laboratory
P. O. Box 73
Lexington, Massachusetts 02173
Attn: Dr. H. I. Smith 1